Inorganic Chemistry

Article

pubs.acs.org/IC

# Site-Selective X-ray Spectroscopy on an Asymmetric Model Complex of the [FeFe] Hydrogenase Active Site

Nils Leidel,[†] Petko Chernev,[†] Kajsa G. V. Havelius,[†] Salah Ezzaher,[‡] Sascha Ott,[‡] and Michael Haumann*[,†]

[†]Freie Universität Berlin, Institut für Experimentalphysik, 14195 Berlin, Germany

[‡]University of Uppsala, Department of Chemistry, Ångström Laboratories, 75120 Uppsala, Sweden

Supporting Information

**ABSTRACT:** The active site for hydrogen production in [FeFe] hydrogenase comprises a diiron unit. Bioinorganic chemistry has modeled important features of this center, aiming at mechanistic understanding and the development of novel catalysts. However, new assays are required for analyzing the effects of ligand variations at the metal ions. By high-resolution X-ray absorption spectroscopy with narrow-band X-ray emission detection (XAS/XES = XAES) and density functional theory (DFT), we studied an asymmetrically coordinated [FeFe] model complex, $[(CO)_3Fe^I1\text{-}(bdtCl_2)\text{-}Fe^I2(CO)(Ph_2P{-}CH_2{-}NCH_3{-}CH_2{-}PPh_2)]$ (**1**, bdt = benzene-1,2-dithiolate), in comparison to iron−carbonyl references. K$\beta$ emission spectra (K$\beta^{1,3}$, K$\beta'$) revealed the absence of unpaired spins and the low-spin character for both Fe ions in **1**. In a series of low-spin iron compounds, the K$\beta^{1,3}$ energy did not reflect the formal iron oxidation state, but it decreases with increasing ligand field strength due to shorter iron-ligand bonds, following the spectrochemical series. The intensity of the valence-to-core transitions (K$\beta^{2,5}$) decreases for increasing Fe-ligand bond length, certain emission peaks allow counting of Fe-CO bonds, and even molecular orbitals (MOs) located on the metal-bridging bdt group of **1** contribute to the spectra. As deduced from 3d → 1s emission and 1s → 3d absorption spectra and supported by DFT, the HOMO−LUMO gap of **1** is about 2.8 eV. K$\beta$-detected XANES spectra in agreement with DFT revealed considerable electronic asymmetry in **1**; the energies and occupancies of Fe-d dominated MOs resemble a square-pyramidal Fe(0) for Fe1 and an octahedral Fe(II) for Fe2. EXAFS spectra for various K$\beta$ emission energies showed considerable site-selectivity; approximate structural parameters similar to the crystal structure could be determined for the two individual iron atoms of **1** in powder samples. These results suggest that metal site- and spin-selective XAES on [FeFe] hydrogenase protein and active site models may provide a powerful tool to study intermediates under reaction conditions.

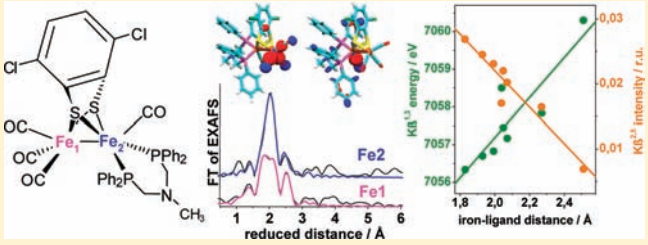


## INTRODUCTION

The foreseeable exhaustion of fossil fuels and progressing climate change call for the development of alternative renewable energy resources.[1] Particularly promising are systems for solar fuel generation,[2−7] wherein, powered by sunlight, "energized" electrons from water oxidation reduce protons to molecular hydrogen ($H_2$). In Nature, both half-cell reactions are catalyzed efficiently at transition-metal active sites in proteins.[2] Light-driven water oxidation at the manganese−calcium complex in photosystem II yields electrons, protons, and $O_2$,[8−10] and $H_2$ turnover occurs at iron- and nickel-containing centers in hydrogenases.[11−14] Biological and biophysical investigations on the enzymes have led to a widespread interest and significant advances in the understanding of polymetallic species in general. The natural active sites may provide blueprints for the design of new synthetic catalysts.[15−19]

In the last decades, synthetic chemistry has succeeded in the biomimetic modeling in particular of the active site of the superior natural $H_2$ producers, the [FeFe]-hydrogenases, aiming at improved understanding of the protein system and at the development of novel catalysts.[15,17,20−24] In the enzymes, a thiolate-bridged binuclear iron site ($2Fe_H$), which is the actual $H^+/H_2$ interconversion catalyst, is linked to a [4Fe4S] iron−sulfur center in the so-called H-cluster (Figure 1).[12,25,26] Today, a wealth of [FeFe] model complexes is available, which address structural features mainly of the $2Fe_H$ subcomplex.[15,17,20−22,27] Unfortunately, their $H_2$ production activity and stability mostly is too low for applications.[28] Possible reasons for these shortcomings include the insufficient characterization and verification of the desired effects of metal-ligation changes.

Crystal structures of [FeFe] compounds do not necessarily provide a mechanistic understanding of the catalytic reactions that usually occur in solution and involve redox chemistry, protonation dynamics, and nuclear rearrangements at the iron atoms and their ligand environment.[18,29−31] Furthermore, direct atomic-level information on the individual metal ions (site selectivity) in, for example, binuclear complexes in noncrystalline materials is difficult to obtain by most

**Received:** November 9, 2011
**Published:** March 23, 2012

   dx.doi.org/10.1021/ic2024154 | Inorg. Chem. 2012, 51, 4546−4559

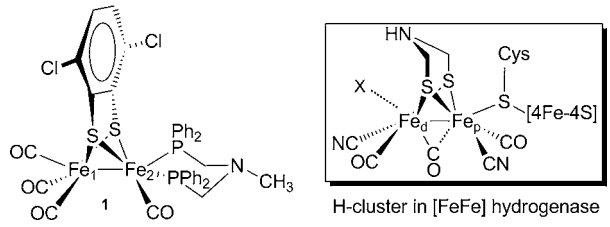


**Figure 1.** Comparison of the structures of complex **1** ($Cl_2bdtFe_2(CO)_4(Ph_2P{-}CH_2{-}NCH_3{-}CH_2{-}PPh_2)$, bdt = benzene-1,2-dithiolate) and the active site of [FeFe] hydrogenase, denoted as H-cluster. The crystal structure of **1** was previously reported (Figure S1).[67] In the present study, its two asymmetrically coordinated iron atoms are denoted Fe1 and Fe2, as shown in the figure. The structure of the H-cluster, here depicted in its putatively oxidized state, comprises a binuclear unit ($2Fe_H$) and a cubane iron–sulfur cluster ([4Fe4S]) and is based on crystallographic and spectroscopic studies.[25,117,123–126] It may contain a bridging carbonyl connecting the proximal (p) and distal (d) iron atoms and a yet unidentified ligand (X) at $Fe_d$; the assignment of a nitrogen atom in the bridging (i.e., azadithiolate) ligand is based on spectroscopic results;[71] Cys denotes a cysteine side chain from the protein. Protons were omitted in the drawings except for the one at the adt-nitrogen for clarity.

spectroscopic methods even for the solid state. Therefore, novel experimental techniques are required for determining structural and electronic properties of specific metal ions in complex centers and under reaction conditions.

In recent years, technical progress at synchrotron radiation sources has facilitated the study of transition-metal sites by element-specific high-resolution X-ray absorption and emission spectroscopy (XAS, XES) methods in relatively dilute samples of synthetic complexes and even proteins.[32–39] In particular, the combination of XAS and XES techniques in a single experiment (XAES), as used in the present study (Figure 2), has been proposed and employed as a viable tool for gaining both structural and electronic information.[35,40–46] By XAS, interatomic distances (bond lengths), geometry, and oxidation state primarily are determined. XES methods are highly sensitive to the electronic structure, as they probe, for example, interactions between core and valence electronic levels of metals and ligands.[40,41] Therefore, XAES, in principle, offers metal spin- and site-selectivity.[40,47–53] The electronic structure information from XAES basically is similar to the one that could be derived from Mössbauer spectroscopy.[54,55] However, few Mössbauer studies on diiron hydrogenase models have been reported, and for XAES,[56–58] $^{57}$Fe labeling of complexes is not required. XAES mostly has been applied to relatively simple, i.e. octahedral, systems. In the present study, an [FeFe] hydrogenase active-site model that exhibits lower symmetry and spin state is explored.

We employed a Rowland-type spectrometer for monitoring the X-ray fluorescence in the Fe K$\beta$ emission region to obtain fluorescence-detected X-ray absorption near edge (XANES) and extended X-ray absorption fine structure (EXAFS) spectra (Figure 2). After creation of a 1s hole by exciting an electron resonantly into bound levels (e.g., Fe-3d) or into the continuum by the absorbed K-edge X-ray photon, the main K$\beta$ emission (K$\beta^{1,3}$ and K$\beta'$ lines) results from metal 3p → 1s decay processes (Figure 2).[41] Due to strong p-d electronic interactions, the shape and energy of the K$\beta$ lines are modified by the valence and spin state and the nature and geometry of ligands.[40,41,47–53] The ligand sensitivity implies different K$\beta$ emission energies for different metal sites of the same element.

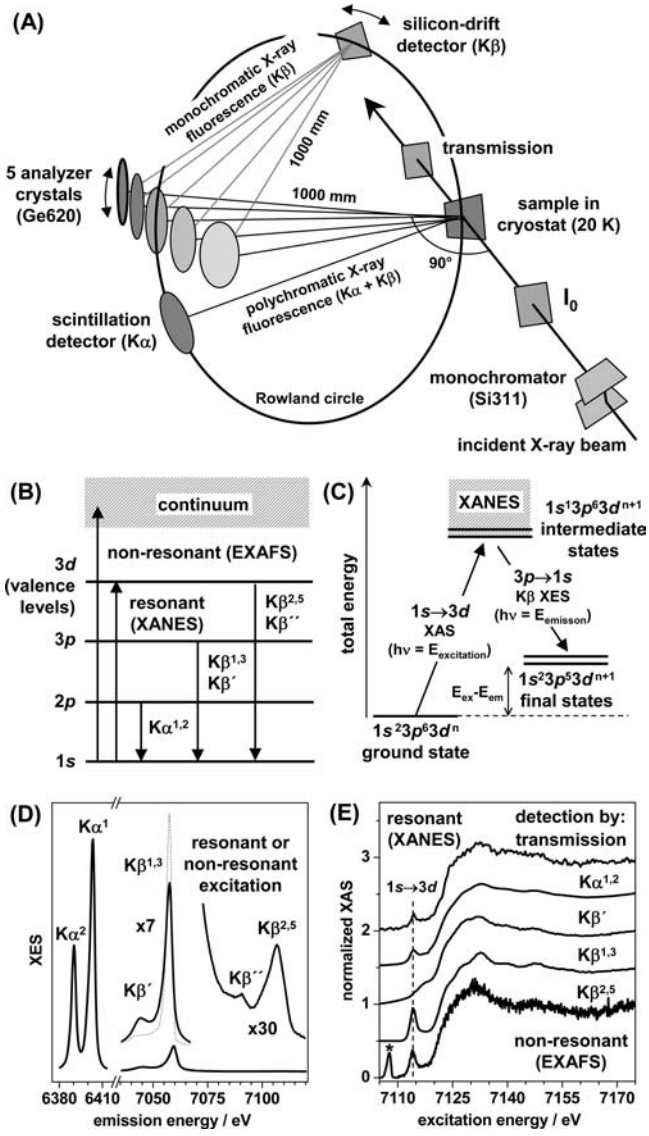


**Figure 2.** Experimental setup for XAES, electronic transitions, and detected signals. (A) Scheme of the Rowland-circle XAS/XES spectrometer. (B) Atomic level energy diagram of electronic excitations due to X-ray absorption and resulting decay processes leading to X-ray fluorescence. (C) State diagram for resonant excitation of 1s → 3d transitions to form intermediate states, which decay by K$\beta$ X-ray fluorescence emission to final state configurations. (D) X-ray emission line spectra of iron for $Fe_3O_4$ as an example (solid lines, data for nonresonant excitation; the scaling of the K$\beta^{2,5}$ peak is relative to the K$\beta^{1,3}$ peak; dotted line, K$\beta$ spectrum for resonant excitation of 1s → 3d transitions at 7114 eV). (E) Fe K-edge spectra of $Fe_3O_4$ measured in absorption mode (transmission) or by X-ray fluorescence detection using the scintillation (K$\alpha^{1,2}$) or silicon-drift (K$\beta$) detectors. The feature in the K$\beta''$ spectrum marked by an asterisk is due to elastic scattering of the excitation beam (down-scaled by a factor of 0.03 for clarity) and reveals the detection bandwidth of ~1 eV.

By measuring XAS spectra using narrow-band K$\beta$ detection, individual metal sites in multinuclear compounds thus may be resolved.[40,47,59–61] Such site-selectivity has been shown, for example, for Prussian blue ($Fe_4[Fe(CN)_6]_3{\cdot}xH_2O$, $x$ = 14–16[62]), allowing for the distinction between the octahedral ($O_h$) low-spin $Fe^{II}(CN)_6$ and high-spin $Fe^{III}(NC)_{4.5}(OH_2)_{1.5}$ centers.[47]


dx.doi.org/10.1021/ic2024154 | Inorg. Chem. 2012, 51, 4546–4559

Comparatively weak emission lines at higher energies, denoted as Kβ satellites (Kβ[2,5] and Kβ″, Figure 2), result from valence-to-core transitions, i.e. decay processes from molecular orbitals (MOs), which are dominated by ligand-s,p and metal-3d contributions.[40,63−65] These features thus probe the chemical properties of the ligands and are affected, for example, by the metal−ligand bond length.[66] It has recently been shown that calculation of Kβ satellites spectra is well feasible by DFT methods,[66] permitting quantitative evaluation of the spectral features.

In the present investigation, a previously synthesized and crystallized [FeFe] hydrogenase model complex, $[Cl_2bdtFe_2(CO)_4(Ph_2P-CH_2-NCH_3-CH_2-PPh_2)]$ (bdt = benzene-1,2-dithiolate)[67] further on denoted as **1** (Figure 1), was studied by XAES methods. Complex **1** features a bidendate phosphine ligand that is coordinated in an asymmetric fashion to one Fe center. The phosphine ligands increase the electron density at the metal site in comparison to the cases of prototypic $[dtFe_2(CO)_6]$ complexes (dt = dithiolate) to an extent that protonation becomes feasible without the need for prior reduction.[67−69] In contrast to symmetric bis-phosphine complexes of type $[dtFe_2(CO)_4(PMe_3)_2]$, for which protonation products have only been observed as bridging-hydride complexes, the asymmetry in **1** promotes the formation of terminal hydride ligands.[70] Terminal hydrides bound to the Fe center distal to the [4Fe4S] cluster are widely believed to be essential for efficient $H_2$ catalysis in [FeFe] hydrogenases.[21,25,71−73] On the other hand, intermediates in the catalytic cycle that contain an Fe−Fe bridging hydride may represent low energy pitfalls in the reaction path of synthetic [FeFe] compounds.[18,74,75] Together with other factors, such as, for example, the absence of a proton relay, the presence of bridging hydrides is believed to be related to the low turnover rates that are frequently encountered for the synthetic complexes.[67,76,77]

Complex **1** is particularly well suited to study site-selectivity in XAES experiments due to the built-in asymmetric ligation of its two iron atoms (Figure 1). Fe1, besides the two metal-bridging sulfur atoms, is coordinated by three carbon monoxide (CO) ligands, whereas Fe2 is ligated by only one CO and two $PPh_3$ groups. Accordingly, the mean Fe-ligand bond lengths is 1.99 Å for Fe1 and longer, 2.15, Å for Fe2; the Fe−Fe distance is 2.54 Å (Figure 1). However, both Fe sites in **1** show a rather regular square-pyramidal geometry ($C_{4v}$) because the dichlorobenzole ring enforces a large distance between the μS atoms of 2.69 Å. In the all-carbonyl analogue $Fe_2S_2(CO)_6$,[78] there exists a covalent bond between the μS atoms (2.08 Å) and, hence, more distorted $C_{4v}$ symmetry, but almost identical mean Fe-ligand distances for the two Fe atoms (1.98 Å) are observed; the Fe−Fe distance is slightly longer, 2.56 Å (Supporting Information Figure S1).

For complex **1** and further iron−carbonyl compounds, we report Kβ emission spectra and Kβ-detected X-ray absorption spectra, interpret the spectra on the basis of DFT calculations, and establish correlations to the ligand field strength and Fe-ligand bond length. The asymmetric electronic structure of **1** became apparent in the MO configurations and energies, allowing, for example, estimation of the highest occupied MO (HOMO)−lowest unoccupied MO (LUMO) energy gap. For both the XANES and EXAFS spectral regions, site-selectivity is demonstrated, yielding structural and electronic parameters for the two individual Fe ions in **1**. These results pave the road for XAES investigations on [FeFe] compounds and hydrogenase proteins, aiming at site-specificity in reaction intermediates.

## MATERIALS AND METHODS

**Synthesis and Sample Preparation Procedures.** Complex **1**, $[Cl_2bdtFe_2(CO)_4(Ph_2P-CH_2-NCH_3-CH_2-PPh_2)]$ (bdt = benzene-1,2-dithiolate), was synthesized and characterized using previously established procedures.[67] The crystal structure of **1** has been reported elsewhere.[67] Compounds used for comparison (pyrite ($FeS_2$), diiron-nonacarbonyl ($Fe_2(CO)_9$), bis(dicarbonyl-*cyclo*-pentadienyl-iron) ($Fe_2(cp)_2(CO)_4$), diethyldithiocarbamic-acid ferric salt ($Fe^{III}(dedtc)_3$)) were purchased (from Sigma-Aldrich or ABCR, Germany) or synthesized using previously established procedures (complex **2** = $[Fe_2(\mu\text{-adt-}CH_2-Ph)(CO)_4(PMe_3)_2]$, adt = S-$CH_2$−NBz-$CH_2$−S;[79] $Fe_2S_2(CO)_6$[80]). Dry powder samples of **1** and the other compounds were homogeneously diluted with boron nitride powder, and the mixtures were filled into Kapton-covered sample holders for the X-ray experiments and frozen in liquid nitrogen.

**X-ray Experiments.** X-ray spectroscopy was carried out at undulator beamline ID26 (http://www.esrf.eu/UsersAndScience/Experiments/DynExtrCond/ID26/) of the European Synchrotron Radiation Facility (ESRF) at Grenoble (France). Samples were held in a laboratory-built liquid-He cryostat at 20 K at an angle of 45° to the incident X-ray beam. The incident energy was set by an Si(311) double-crystal monochromator (energy bandwidth ∼0.2 eV at the Fe K-edge). Higher harmonics were suppressed by two Si-coated mirrors working at 2.5 mrad in total reflection. The X-ray spot size on the sample was about 1 (horizontal) × 0.5 (vertical) $mm^2$ as set by slits; the X-ray flux at the sample position was about $10^{13}$ photons $s^{-1}$ $mm^{-2}$. Conventional XAS spectra were collected by monitoring the Kα fluorescence using a scintillation detector[38] (∼20 $cm^2$ area, placed at 90° to the incident X-ray beam and at ∼1 m to the sample), which was shielded by 10 μm Mn foil against scattered incident X-rays, or in standard transmission mode (absorption spectra). High energy-resolution emission detection was achieved by using a vertical-plane Rowland-circle spectrometer (Figure 2). A silicon-drift detector (SDD) was used for monitoring of the fluorescence, with a slit opening of 1 mm in front of it. A total energy bandwidth of ∼1.0 eV at the Fe Kβ fluorescence line was achieved using the [620] Bragg reflection of five spherically bent Ge wafers ($R$ = 1000 mm). The energy axis of the monochromator was calibrated by using a Gaussian fit to the peak feature at 7112 eV in the first derivative of the absorption spectrum of an Fe foil, corresponding to the first inflection point in the K-edge rise, as a reference. The energy axis of the emission spectrometer was calibrated using a Gaussian fit to the elastic scattering peak of the incident X-ray beam as measured by the SDD. The calibration accuracy was estimated as ±0.1 eV. XAS spectra at the Fe K-edge were measured for a monochromator scan range of 6950−7150 eV, i.e. for a $k$-range of up to ∼16 $Å^{-1}$, using the rapid-scan mode of ID26 (simultaneous scanning of the monochromator and of the gaps of two undulators) and a total scan duration of 60 s (3000 data points with an energy spacing of ∼0.066 eV, 20 ms acquisition time per data point). Extensive XAS data averaging was employed to improve the signal-to-noise ratio (up to 100 scans, each measured on a fresh sample spot). The absence of radiation damage was ensured by attenuation of the incident X-ray beam (if necessary, using an Al filter foil box from XIA) to a level at which no changes in the XANES spectra could be detected for consecutive XAS scans on the same sample spot. Kβ emission line spectra were collected for off-resonance excitation (7700 eV) and scanning of the emission energy in 0.35 eV steps over the main line (7035−7070 eV) and satellite line (7070−7130 eV) regions on separate sample spots (0.5 s acquisition time per data point). During spectrometer movements to change the detection energy, a rapid shutter blocked the incident X-ray beam. The absence of radiation damage was achieved by beam attenuation (see above) and measuring of XANES spectra, which were identical prior to and after the Kβ line measurements (not shown). Up to 30 emission line scans were averaged for signal-to-noise improvement. Shown Kβ line spectra represent the intensity ratio of $I_{SDD}/I_0$ ($I_0$ was measured with a


dx.doi.org/10.1021/ic2024154 | Inorg. Chem. 2012, 51, 4546−4559

**Table 1. General Structural and Electronic Properties of the Used Iron Compounds**

| iron compound[a] | first-sphere ligation | geometry | formal oxidation state | spin state | crystal structure ref |
|---|---|---|---|---|---|
| **1**[b] | $S_2(CO)_3$ (Fe1) $S_2P_2(CO)$ (Fe2) | $C_{4v}$ | I,I | low-spin | 67 |
| **2**[c] | $S_2P(CO)_2$ | $C_{4v}$ | I,I | low-spin | 79 |
| $Fe_2S_2(CO)_6$ | $S_2(CO)_3$ | $C_{4v}$ | I,I | low-spin | 78 |
| $Fe_2(CO)_9$ | $(CO)_6$ | $O_h$ | 0,0 | low-spin | 127 |
| $Fe_2(cp)_2(CO)_4$ | $(cp)(CO)_3$ | $T_d$ | II,II | low-spin | 128 |
| $FeS_2$ | $S_6$ | $O_h$ | II | low-spin | 129 |
| $Fe(dedtc)_3$[d] | $S_6$ | $O_h$ | III | low-spin[e] | 130 |
| $[Fe(CN)_6]^{4-}$ | $(CN)_6$ | $O_h$ | II | low-spin | 131 |
| $[Fe(tacn)_2]^{2+}$[f,g] | $N_6$ | $O_h$ | II | low-spin | 132 |
| $[FeCl_6]^{4-}$[g] | $Cl_6$ | $O_h$ | II | high-spin | 133 |

[a]For crystal structures of the compounds, see Supporting Information (Figure S1). [b]**1** = $[Cl_2bdtFe_2(CO)_4(Ph_2P{-}CH_2{-}NCH_3{-}CH_2{-}PPh_2)]$ (bdt = benzene-1,2-dithiolate). [c]**2** = $[Fe_2(\mu\text{-adt-}CH_2{-}Ph)(CO)_4(PMe_3)_2]$ (adt = $S{-}CH_2{-}NBz{-}CH_2{-}S$). [d]dedtc = diethyldithiocarbamate. [e]low-spin Fe(III) at 20 K.[122] [f]tacn =1,4,7-triazacylononane. [g]Data for these compounds were taken from ref 66.

scattering foil and photodiode detector closely in front of the sample); spectra were normalized to unity value of the whole area under the K$\beta$ line spectra. XAS spectra, after signal averaging, were normalized and EXAFS oscillations were extracted as previously described.[81] The energy scale of the EXAFS spectra was converted to a wavevector ($k$) scale using an $E_0$ value of 7112 eV. Unfiltered $k^3$-weighted spectra were used for least-squares curve-fitting, including multiple-scattering paths up to third order, and Fourier-transform (FT) calculation with the in-house program SimX.[81] FTs were calculated using $\cos^2$ windows extending over 10% at both $k$-range ends. In EXAFS simulations, phase-functions calculated with FEFF8 (group of J. J. Rehr, University of Washington, http://leonardo.phys.washington.edu/feff/) and an amplitude reduction factor ($S_0^2$) of 0.85 were used. $E_0$ was refined to ~7120 eV in the EXAFS simulations.

**Scattering Theory K-Edge Simulations.** XANES calculations were performed as described previously[30,82] using FEFF8[83] with the full-multiple-scattering (FMS) and the self-consistent-field (SCF) options activated. Atomic coordinates of FEFF input files were based on the respective crystal structures (Table 1). Calculated XANES spectra were shifted by 4 eV to lower energies. No further attempts were made to improve the matching between experimental and calculated XANES spectra.

**Density Functional Theory Calculations.** Spin-unrestricted DFT single-point calculations were performed with the ORCA program package.[84] The BP86 or B3LYP exchange correlation functionals[85−87] and a triple-$\zeta$ valence plus polarization (TZVP) basis set[88] were used. The resolution of the identity (RI) approximation and tight self-consistent field convergence criteria were employed. The crystal structure of **1** was used with a total charge of zero and a singlet ground state. The resulting MOs were visualized as isosurfaces using cutoff values of 0.4 or 0.04. To evaluate the contributions of the individual Fe-d atomic orbitals to each MO, the following procedure was applied. First, the MO with highest Fe d($z^2$) character was identified by visual inspection of the MOs around the HOMO−LUMO gap; it was found that this MO was roughly aligned along the Fe−Fe axis as expected. Then, the atom coordinates of the complex were rotated so that this axis pointed in the $z$-coordinate direction and the Fe ligands were located roughly in the $xz$ and $yz$ planes. With the oriented structure, the single-point calculation was then repeated and Mulliken population analysis[89] was performed as implemented in ORCA.[84] X-ray absorption K-edge intensities in the pre-edge and rising-edge regions were calculated using the time-dependent DFT (TD-DFT) formalism.[90] Electronic transitions from each of the two Fe-1s orbitals to the lowest 200 unoccupied MOs were considered. Magnetic dipole and electric quadrupole contributions to the spectrum were also taken into account. K$\beta$ valence-to-core (K$\beta^{2,5}$) spectra were calculated on the basis of the crystal structures of compounds and assuming a spin multiplicity of 1, using the BP86 functional and a TZVP basis set. After the ground state DFT calculation, TD-DFT calculations for each individual Fe atom were performed. Shifts to higher energies by 181.5 and 1.0 eV Gaussian broadening were applied to calculated K$\beta$ stick spectra for comparison with experimental data. MOs were visualized using UCSF Chimera or Jmol.

## RESULTS AND DISCUSSION

**Iron Compounds Investigated and Experimental Setup.** This investigation focuses on an [FeFe] model complex (**1**, $Cl_2bdtFe_2(CO)_4(Ph_2P{-}CH_2{-}NCH_3{-}CH_2{-}PPh_2)$, bdt = benzene-1,2-dithiolate),[67] which includes several structural features of the active site of [FeFe] hydrogenases, i.e. carbonyl (CO) ligands at the square-pyramidal Fe ions, a bridging-thiolate containing central group, and a pendant nitrogen base in the second coordination sphere (Figure 1). The intrinsic asymmetry of the iron ligation in **1** ($S_2(CO)_3$ for Fe1, $S_2P_2(CO)$ for Fe2) renders this compound ideally suited for high-resolution XAES, that is the combination of X-ray absorption (XAS) and emission (XES) spectroscopy, aiming at site-selectivity. In addition, several iron reference compounds were studied in comparison, some properties of which are listed in Table 1 (for respective crystal structures, see Figure S1). In Figure 2, the setup of the XAES experiment is depicted schematically, together with the relevant electronic excitation and decay processes and examples of the resulting spectra (for $Fe_3O_4$).

**K$\beta$ Emission Spectra.** Iron K$\beta$ main line and satellite emission spectra for nonresonant excitation of **1** are compared to spectra of the more symmetric [FeFe] model complexes **2**[79] and $Fe_2S_2(CO)_6$, and of further reference compounds in Figure 3. Similar K$\beta^{1,3}$ line shapes were observed for all compounds, irrespective of the varying iron ligation (Table 1). However, the K$\beta^{1,3}$ line energies differ. Spectral features in the K$\beta'$ region, which are prominent for high-spin Fe(II) and Fe(III) species,[48,66] are absent for **1**, similar to the case of the references (Figure 3A).

*Apparent Spin State and Coordination Symmetry.* The K$\beta'$ emission is a spin-polarization feature and mostly explained by Fe(3p,3d) exchange coupling between unpaired metal 3d spin-up (spin-down) electrons and a spin-up (spin-down) hole in the 3p level in the final state[52,91−93] (Figure 4). The intensity of the K$\beta'$ line thus decreases with a decrease in the number of unpaired 3d electrons, i.e. with the effective spin state, as has been shown for various first-row transition metal compounds with increasing oxidation state.[40,50,53,94] For the case of nonresonant excitation, multiplet calculations on the K$\beta$ transitions for high-spin $O_h$ Mn or Fe have revealed that for systems with only 3d spin-up electrons (e.g., Fe(III)-$d^5$, $S$ =


dx.doi.org/10.1021/ic2024154 | Inorg. Chem. 2012, 51, 4546−4559

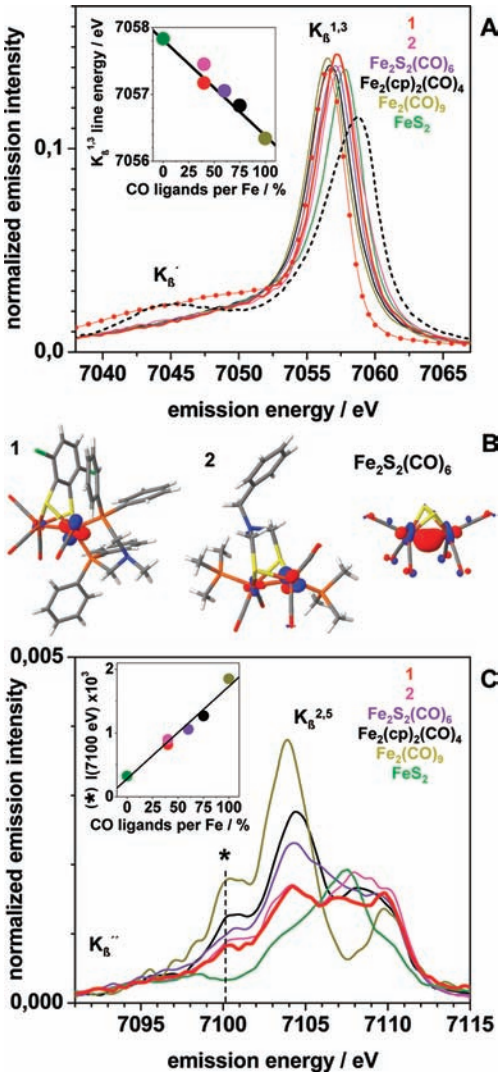


**Figure 3.** X-ray emission spectra in the K$\beta$ region for nonresonant excitation. (A) Spectrum of **1** (see Figure 1) in the K$\beta^{1,3}$ and K$\beta'$ regions (red line) compared to spectra of low-spin reference compounds (see Table 1 and Supporting Information Figure S1 for details; **2** denotes [$Fe_2$($\mu$-adt-$CH_2$–Ph)(CO)$_4$($PMe_3$)$_2$)] (adt = S–$CH_2$–NH–$CH_2$–S)[79]). Red dots represent the spectrum of **1** for resonant excitation at 7113 eV of 1s → 3d transitions (see Figure 7). The black dashed line shows the spectrum of $Fe^{II}O$. Inset: respective K$\beta^{1,3}$ line energies as derived from the zero-crossing points in the first derivative spectra (not shown) plotted versus the percentage of CO ligands at the 4-, 5-, or 6-coordinated Fe ions. (B) Localization of the HOMO in complexes **1**, **2**, and $Fe_2S_2(CO)_6$. (C) Spectra in the K$\beta$ satellites region (K$\beta^{2,5}$ and K$\beta''$); the background from the high-energy tail of the K$\beta^{1,3}$ lines was approximated by a third order polynomial and subtracted from all spectra. The asterisk and vertical dashes mark the energies for which the amplitudes of spectra are plotted in the inset. Spectra in parts A and C were normalized to unity values of their integral intensities in the whole K$\beta$ emission region.

$^5/_2$), the K$\beta'$ line reflects almost exclusively the $3p^5$ spin-up hole state, whereas both $3p^5$ spin-up and spin–down hole states contribute to the K$\beta^{1,3}$ emission.[52,91] For low-spin $O_h$ Fe(II)-$d^6$ compounds, the K$\beta'$ feature is absent,[66] as explained by the absence of unpaired 3*d* electrons (Figure 4). This is in agreement with the spectrum of, for example, low-spin Fe(II)[95] in $FeS_2$ (Figure 3A).

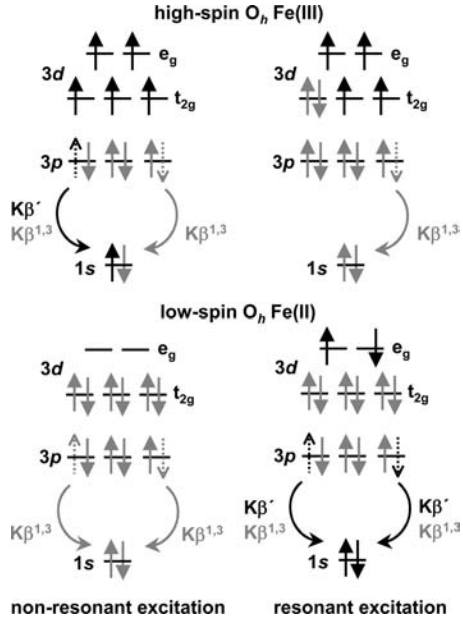


**Figure 4.** Final state electronic configurations and K$\beta$ emission. After excitation into the continuum (nonresonant, left) or the 3*d* levels (resonant, right), spin-up or –down holes are created in the 3*p* shell upon intermediate state decay, accompanied by K$\beta$ fluorescence emission. Alternative spin configurations are shown in the same chart where applicable. Only for interaction of 3p holes and unpaired 3d electrons with the same spin flavor, fluorescence in the K$\beta'$ region is observed (black); otherwise only K$\beta^{1,3}$ emission results (gray). This simplistic view rationalizes the observed spin-selectivity in the XAES data.

**Table 2. Some Electronic Features of Complexes 1, 2, and $Fe_2S_2(CO)_6$ from DFT**

| parameter/complex | 1 | 2 | $Fe_2S_2(CO)_6$ |
|---|---|---|---|
| Mulliken charge (Fe1, Fe2) | 0.20, 0.11 | 0.17, 0.13 | 0.27, 0.26 |
| HOMO[a] energy [eV] | −4.734 | −4.654 | −6.222 |
| HOMO Fe-character (Fe1, Fe2)[b] [%] | 5.8, 71.5 | 14.8, 51.2 | 34.9, 35.2 |

[a]Fe1 and Fe2 refer to the iron atoms depicted on the right or left sides in the structures shown in Figure 3B. The spins were practically zero for all iron species. DFT results are for the BP86/TZVP theory level. [b]HOMO = highest (double) occupied molecular orbital; MO structures and energies for spin-up and spin-down states are identical.

For a square-pyramidal ($C_{4v}$) Fe geometry (neglecting a possible Fe–Fe bond) and the presence of strong CO ligands as in **1**, large crystal field splitting and therefore decreased d-orbital degeneracy compared to $O_h$ symmetry are expected. The formal Fe(I)Fe(I) oxidation state ($d^7$) of **1** might lead to an apparent increase in the effective spin state and to an increased K$\beta'$ feature. The small K$\beta'$ emission (Figure 3A) thus suggests a low-spin state and the absence of unpaired 3*d* electrons, for both Fe ions of **1**. This holds true also for the more symmetric diiron complexes **2** ($Fe^I_2$), $Fe^I_2S_2(CO)_6$, $Fe^0_2(CO)_9$, and $Fe^{II}_2(cp)_2(CO)_4$ (Figure 3A). The effect of an additional unpaired electron in the 3d levels, on the other hand, is nicely exemplified by the pronouncedly increased K$\beta'$ emission in the spectrum of **1** (Figure 3A), which is observed for resonant excitation of 1s → 3d transitions in the pre-edge absorption region (see Figure 7).

For the diiron complexes formally containing two Fe(I) ions, the apparent absence of unpaired 3*d* spins should reflect spin-


dx.doi.org/10.1021/ic2024154 | Inorg. Chem. 2012, 51, 4546–4559

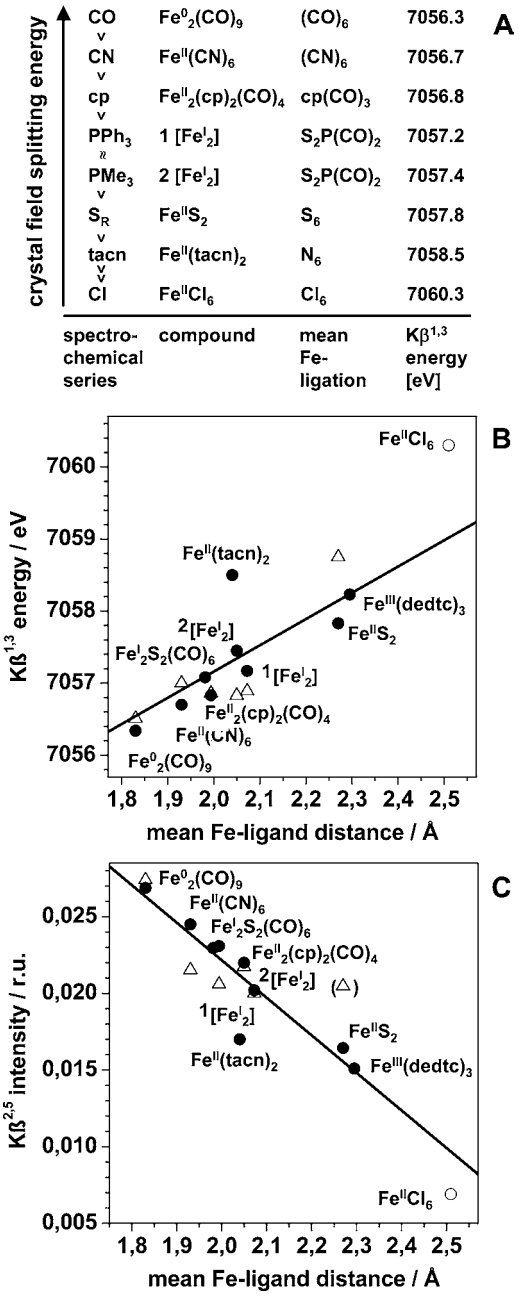


**Figure 5.** Correlations between iron ligation and K$\beta$ emission properties. (A) The K$\beta^{1,3}$ line energy of the low-spin Fe compounds decreases in good agreement with the spectrochemical series for increasing average crystal-field splitting capability (field strength) of the ligands, but not according to the formal oxidation states. $Fe^{III}(dedtc)_3$ is a trivalent species, $[Fe^{II}Cl_6]^{4-}$ is a high-spin example. (B) The K$\beta^{1,3}$ energy (Figure 3A) increases for increasing mean Fe-ligand distance as derived from the crystal structures (see Table 1 and Figures 1 and. S1). (C) The integrated intensity in the K$\beta^{2,5}$ region (Figure 3B) decreases for increasing mean Fe-ligand distance. Open triangles in (B) and (C) represent values calculated by DFT (K$\beta^{1,3}$ energies shifted by 3.4 eV to lower values, K$\beta^{2,5}$ intensities divided by a factor of 1.5 for comparison with the experimental data); the calculated value for the K$\beta^{2,5}$ area of $FeS_2$ (in parentheses) likely is overestimated by the DFT approach for this bulk material. Lines in (B) and (C) are linear regressions to the experimental data. Values for $[Fe^{II}Cl_6]^{4-}$ and $[Fe^{II}(tacn)_2]^{2+}$ were taken from ref.,[66] data for $[Fe^{II}(CN)_6]^{4-}$ were identical in the present study and in ref 66.

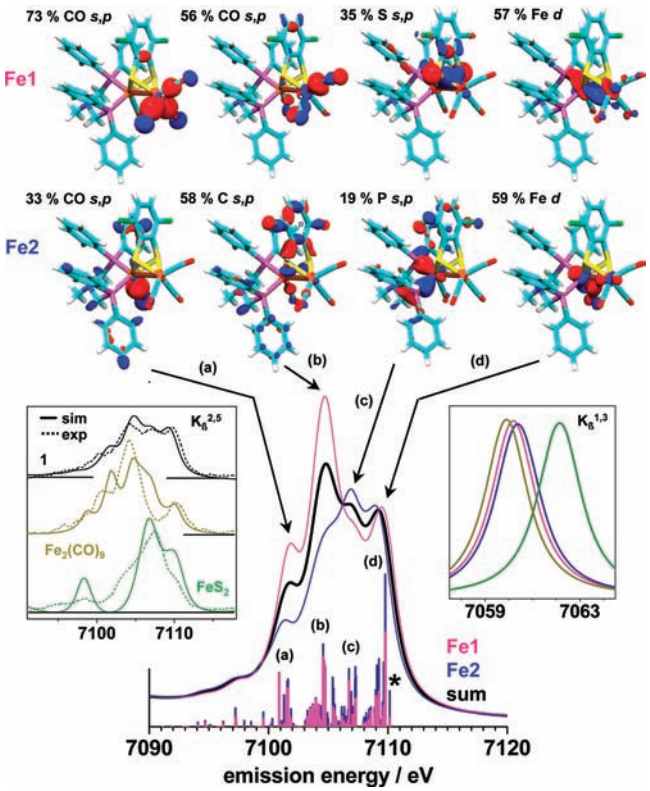


**Figure 6.** K$\beta$ emission lines and molecular orbitals calculated by DFT. The calculated emission spectrum in the K$\beta^{2,5}$ region of **1** was derived by Gaussian broadening (fwhm = 1 eV) of the stick spectra for the two iron atoms (Fe1, magenta; Fe2, dark-blue; the asterisk marks the HOMO → 1s transition) and averaging of the two spectra (black line). Calculated spectra are normalized to unity area in the whole K$\beta$ region. In the left inset, calculated (solid lines) and experimental (dashed lines), K$\beta^{2,5}$ spectra for the indicated compounds are compared. The right inset shows the corresponding calculated K$\beta^{1,3}$ spectra. The MOs for Fe1 and Fe2 of **1**, corresponding to the sticks labeled (a, b, c, d), are shown in the top part of the figure together with the structure of **1** and the most prominent atomic orbital (AO) contributions.

pairing in the HOMO, which, depending on the coordination symmetry, may be delocalized over both Fe ions or more localized on one Fe site, i.e. resembling an electronic configuration closer to Fe(0)Fe(II). For the asymmetric complex **1**, the HOMO (Figure 3B) is calculated by DFT to be almost localized on Fe2. Slightly higher delocalization is observed for the more symmetric complex **2** and complete delocalization occurs in $Fe_2S_2(CO)_6$, for which the two iron atoms are indistinguishable. The Mulliken charges on the iron atoms also are most unevenly distributed for **1** (Table 2). As expected, the total spin is calculated as zero for the three complexes. In summary, the absence of unpaired spins is clearly revealed in the K$\beta$ spectrum of **1**, whereas the coordination asymmetry is apparent in the MO structure, which is analyzed in more detail below.

*K$\beta^{1,3}$ Line Energy and Ligation Strength.* The K$\beta^{1,3}$ line energy decreases about linearly and by ~1.5 eV for an increase of the mean relative number of CO ligands per Fe ion from 0% (i.e., in $FeS_2$) to 100% (in $Fe_2(CO)_9$) in the series of low-spin complexes (Figure 3A, inset). For an Fe(III)→Fe(II) reduction in $[Fe(CN)_6]^{4-}$ and $[Fe(tacn)_2]^{2+}$, a down-shift of the K$\beta^{1,3}$ line by about −0.8 eV has been observed.[66] However, the K$\beta^{1,3}$


dx.doi.org/10.1021/ic2024154 | Inorg. Chem. 2012, 51, 4546–4559

**Table 3. Energy Differences between Fe-3p Dominated MOs and Fe-1s Levels for the Two Iron Atoms of Complex 1 Derived from DFT Calculations[a]**

| Fe-3p AO type and contribution to MO (%) | Fe1-$p_y$ 90 | Fe1-$p_x$ 99 | Fe1-$p_z$ 30, Fe2-$p_x$ 45 | Fe1-$p_z$ 50, Fe2-$p_x$ 35 | Fe2-$p_y$ 60, Fe2-$p_z$ 35 | Fe2-$p_z$ 50, Fe2-$p_y$ 40 |
|---|---|---|---|---|---|---|
| $\Delta E$[(MO) − $E$(Fe1-1s)] (eV) | −0.25 | −0.13 | 0.23 | 0.27 | 0.56 | 0.89 |
| $\Delta E$[(MO) − $E$(Fe2-1s)] (eV) | −0.75 | −0.63 | −0.27 | −0.23 | 0.06 | 0.39 |
| mean $\Delta E$ (eV) | −0.50 | −0.38 | −0.02 | 0.02 | 0.31 | 0.64 |

[a] $\Delta E$ values were centered around zero by subtraction of the mean value for the four MOs with contributions from both Fe1 and Fe2.

energy is 7056.8 eV for $[Fe^{II}(CN)_6]^{4-}$, similar to $Fe^0{}_2(CO)_9$, and by 1.7 eV higher for $[Fe^{II}(tacn)_2]^{2+}$. For $Fe^{II}{}_2(cp)_2(CO)_4$ and $Fe^{II}S_2$ the K$\beta^{1,3}$ energies differ by ∼1 eV (Figure 3A). Accordingly, the K$\beta^{1,3}$ energy is not proportional to the formal iron oxidation state. It also seems not to be very sensitive to changes of the coordination symmetry or to a change from mono- to binuclear complexes (Table 1). Empirically, the K$\beta^{1,3}$ energy rather appears to decrease with increasing average field strength of the ligands according to the well-known spectrochemical series.[96−98] For the dominance of strong-field ligands such as CO, a low K$\beta^{1,3}$ energy was observed for the low-spin iron compounds and such a relation may also hold for high-spin species (Figure 5A). In tendency, the K$\beta^{1,3}$ energy increased for an increasing mean Fe-ligand bond length (Figure 5B). These relations seem not to be much affected by the presence of bridging or terminal CO ligands.

For strong-field ligands (CO) and respective short Fe-ligand bonds, a large crystal field energy splitting (10 Dq) is expected.[99,100] This means that the K$\beta^{1,3}$ energy, or in other words, the 3p-1s energy difference, seems to decrease for an increasing value of 10 Dq. The $\sigma$-bond strength, which increases the electron density at the iron, rather than the $\pi$-backbonding having the opposite effect, may account for a lowering of the 3p level energies and thus for a lower K$\beta^{1,3}$ energy, at least for low-spin compounds. The K$\beta^{1,3}$ energy thus should be related to the Fe-ligand bond covalency and to the redox potential, as modified, for example, by ligand exchanges.[56,101−105] Accordingly, it may provide an assay for the probing of ligand exchange effects on the bonding and redox properties of the metal centers in [FeFe] hydrogenase active site models. In addition, the dependence of the K$\beta^{1,3}$ energy on the ligand environment facilitates site-selective XAES, as demonstrated further below.

*Valence-to-Core Transitions.* The low-intensity K$\beta^{2,5}$ spectra due to valence-to-core transitions in **1** and selected references are shown in Figure 3C. Notably, spectral features in the K$\beta''$ region are absent for the low-spin iron compounds. Visual inspection revealed at least four K$\beta^{2,5}$ maxima. The amplitudes of the two maxima at lower energies roughly correlate with the number of CO ligands per Fe (Figure 3C, inset), a peak at ∼7108 eV is more prominent in compounds with Fe−S,P bonds, and the feature at the highest energy is similar in the molecular systems and diminished for $FeS_2$. This shows that approximate counting of ligand species is feasible already by qualitative evaluation of K$\beta^{2,5}$ spectra. The maximum at the highest energy is mostly due to decay processes from MOs which are dominated by Fe-d contributions (see next section). Its energy is rather similar (∼7110.5 eV) in compounds with formal iron oxidation states of 0, I, and II (Figure 3A). For an Fe(II) → Fe(III) oxidation in $[Fe(CN)_6]^{4-}$ and $[Fe(tacn)_2]^{2+}$ an upshift of the K$\beta^{2,5}$ energy by ∼1.4 eV has been reported.[66] This reinforces that the energy of the 3d → 1s transitions does not reflect the formal Fe oxidation state in the low-spin species but rather is adjusted mainly by the iron−ligand bond strength.

In a previous study, an increase of the total K$\beta^{2,5}$ intensity for shorter metal−ligand bonds has been calculated and rationalized by increasing ligand/Fe-np orbital mixing.[66] Indeed, an increase of the integrated K$\beta^{2,5}$ intensity for a decreasing mean Fe−ligand distance was observed for the low-spin compounds (Figure 5C), which could be qualitatively reproduced by the DFT calculations. That the intensities of the Fe-3d → Fe-1s transitions at the highest energies decrease for the centrosymmetric ($O_h$) systems ($FeS_2$, $Fe(tacn)_2$, $K_4Fe(CN)_6$) is explained by the decreased admixture of Fe-p contributions into the Fe-d dominated MOs. This effect may contribute, for example, to the off-line position of the $Fe(tacn)_2$ data point in Figure 5C.

*HOMO−LUMO Energy Difference.* In principle, the HOMO−LUMO energy difference may be determined from the (3d → 1s) transition at the highest energy in the K$\beta^{2,5}$ emission (Figure 3C) and the (1s → 3d) transition at the lowest energy in the pre-edge absorption of the XANES (Figure 7). For **1**, the respective spectral features were observed at ∼7110.0 eV and ∼7112.8 eV, meaning that the experimental gap is estimated as ∼2.8 eV. Within the considerable uncertainty limits, this value is in agreement with the DFT calculations described further down. We note that determination of the experimental gap may be complicated in particular in cases for which the HOMO → 1s transition and/or the 1s → LUMO transition in the K$\beta^{2,5}$ and XANES spectra shows low oscillator strengths, as expected, for example, for centrosymmetric coordination environments. However, the DFT calculations revealed that both transitions show significant intensities for the distorted $C_{4v}$ symmetry of the iron atoms in **1**.

*DFT Calculation of Kβ Emission Spectra.* Using a previously outlined DFT approach,[66,106] calculations of K$\beta$ spectra were performed (Figure 6). Because of the neglect of electronic relaxation and multiplet effects in the DFT approach, only rough shapes can be calculated for the K$\beta^{1,3}$ lines, but these effects are less important for the K$\beta^{2,5}$ region.[66] However, the experimental trend of decreasing K$\beta^{1,3}$ energy for increasing number of CO ligands could approximately be reproduced (Figures 5 and 6). Good agreement between experimental and calculated K$\beta^{2,5}$ spectra was obtained, in particular for complex **1** (Figure 6). Deviations between calculated and experimental spectra are attributed, for example, to noise contributions to the XES data and to imperfect matching of the relative transition energies from DFT. The calculations verify the conclusions already drawn on the basis of qualitative inspection of the spectra, namely that, for **1**, the two maxima at lowest energies are dominated by decay from MOs with mainly (CO)-s,p contributions, a middle maximum shows mostly S,P-s,p contributions, and the highest-energy maximum reflects the Fe-d levels (Figure 6).

Additional information is obtained by inspection of the Fe-d dominated MOs of **1**. In general, these MOs are relatively


dx.doi.org/10.1021/ic2024154 | Inorg. Chem. 2012, 51, 4546−4559

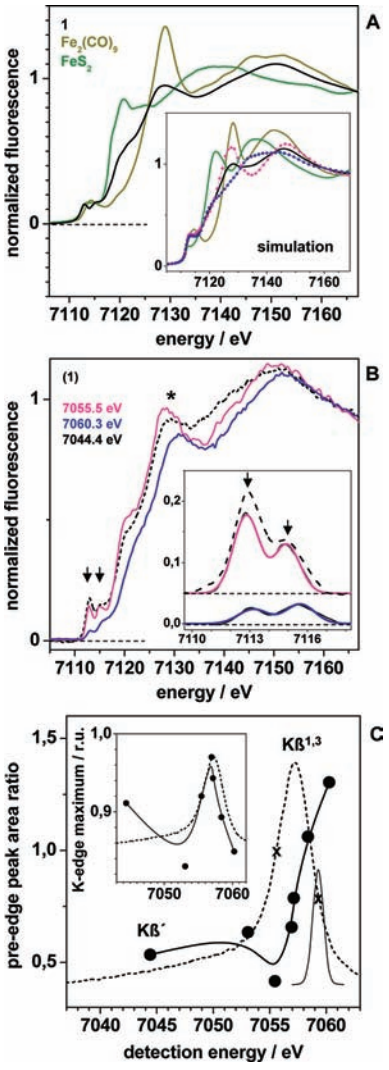


**Figure 7.** XANES analysis for complex **1**. (A) Conventional K$\alpha$-fluorescence detected Fe K-edge spectra of **1** and two reference compounds. The inset shows spectra which were calculated on the basis of crystal structures using scattering theory.[109] For **1**: black line, mean of spectra calculated individually for Fe1 (magenta) and Fe2 (dark-blue). (B) XANES spectra of **1** for the indicated low and high K$\beta^{1,3}$ detection energies. The dashed line represents a spectrum measured for detection in the K$\beta'$ region. Arrows mark the two pre-edge features; the asterisk denotes the primary edge maximum. Inset: respective pre-edge spectra (vertically displaced for comparison) as obtained after subtraction of a polynomial background from the main-edge spectra; black lines, experimental data, colored lines, simulations using the sum of two Gaussian functions (full width at half maximum (fwhm) = 1.7 eV) and the following center energies (areas): 7112.8 eV (0.22) and 7114.9 eV (0.13), magenta; 7113.2 eV (0.07) and 7115.6 eV (0.08), dark blue. The spectral differences likely are attributable to relatively prominent and varying contributions from the two different iron sites as well as to (less prominent) contributions from the underlying electronic multiplet structure (see also Figure 8 and Supporting Information Figures S3). (C) Pre-edge peak area ratios and K-edge maxima in the inset as a function of the detection energy. Data points stem from spectra as in part B (solid circles, experimental data; spline curves were drawn to guide the eye). The K$\beta$ emission spectrum of **1** is shown for comparison (dashed lines); the ~1 eV detection bandwidth is shown by the Gaussian (thin line) for comparison; (x) denotes mean detection energies as used for EXAFS measurements (Figure 10B).

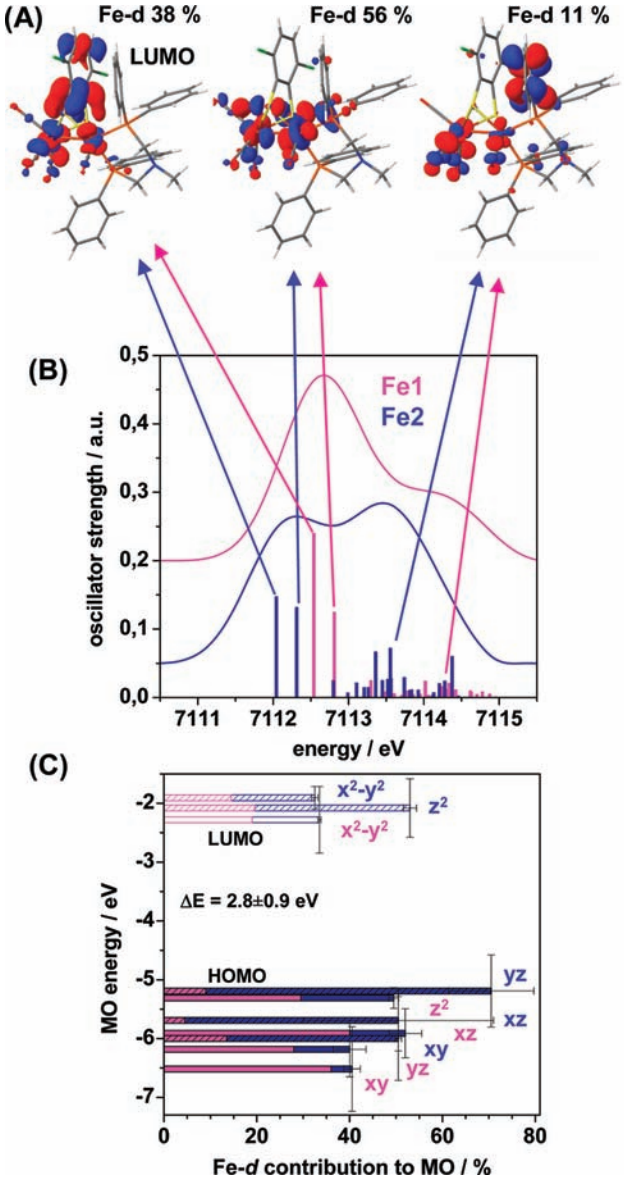


**Figure 8.** DFT results for the pre-edge transitions of **1**. In part A, MO configurations (note the indicated Fe-d contributions from Mulliken analysis; see also Supporting Information Table S1) of selected transitions from Fe-1s levels in the pre-edge region of the Fe K-edge are shown as stick spectra in part B. In part B, also line spectra derived by Gaussian broadening (1.0 eV) and summation over all Gaussians are shown for the two iron atoms (vertically shifted for comparison). Spectra in part B were derived using the BP86 functional in the DFT calculations. (Overall similar line shapes were derived for the B3LYP functional (not shown).) (C) MO energies plotted versus the respective Fe-d contributions (magenta, Fe1-d contributions; dark-blue, Fe2-d contributions; nonhatched and hatched bars denote MOs located preferentially on Fe1 or Fe2; open and solid bars denote unoccupied or double-occupied MOs). The MOs (high to low energy) contain the following Fe-d AO contributions (mean values for BP86 and B3LYP functionals): Fe2-d($x^2 - y^2$) 11%, Fe2-d($z^2$) 21%, Fe1-d($x^2 - y^2$) 13%, Fe2-d($yz$) 39%, Fe1-d($z^2$) 21%, Fe2-d($xz$) 27%, Fe1-d($xz$) 28%, Fe2-d($xy$) 32%, Fe1-d($yz$) 13%, Fe1-d($xy$) 28%. Error bars give the full ranges of energies and total Fe-d contributions as resulting from the use of BP86 or B3LYP functionals in the DFT calculations.

localized on either the Fe1 or Fe2 metal–ligand centers. The Fe-d dominated maximum in the K$\beta^{2,5}$ spectrum of Fe1 is at ~0.5 eV higher energy compared to that of Fe2, as probably


dx.doi.org/10.1021/ic2024154 | Inorg. Chem. 2012, 51, 4546–4559

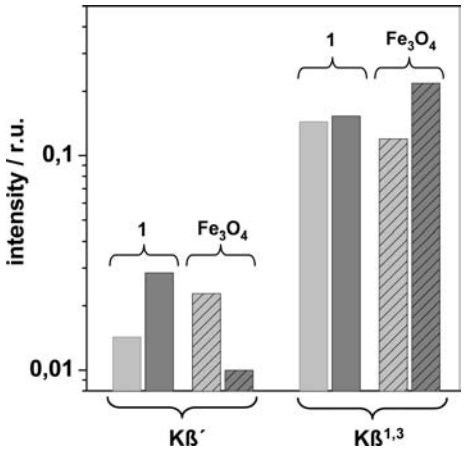


**Figure 9.** Spin-selective XAES at the Fe K-edge. Relative amplitudes of emission maxima in the K$\beta'$ and K$\beta^{1,3}$ spectral regions for nonresonant excitation (7700 eV, light gray) or resonant excitation into the first pre-edge peak (7113.5 ± 0.5 eV, dark gray). Open bars show values for the low-spin complex **1** containing formal Fe(I); hatched bars show values for high-spin $Fe_3O_4$ containing Fe(III) (see Figures 2, 3, and 7 for respective K$\beta$ and XANES spectra); r.u. = relative units; note the logarithmic *y*-axis.

explained by the enhanced $\pi$-backdonation to the CO ligands for Fe1. In particular for Fe2, the spectrum shows considerable contributions from MOs residing on the metal-bridging ligand, meaning that chemical changes even at this relatively remote group may become accessible in the K$\beta^{2,5}$ spectrum. The transition at the highest energy corresponds to decay from the HOMO, which is located mostly (64%) on Fe2 (for calculation using the BP86 functional, see below). The HOMO → 1s transition shows considerable oscillator strength (Figure 6), which supports that estimation of the HOMO energy (relative to the LUMO) from the experimental K$\beta^{2,5}$ spectrum is feasible for **1** (see the previous section).

In conclusion, satisfactory simulation of valence-to-core transitions, in particular for [FeFe] model complexes, is achieved. For bulk materials such as $FeS_2$, the agreement between calculated and experimental spectra may be poorer, possibly due to extended electronic delocalization effects. Experimental and DFT analysis of the K$\beta$ satellites spectra opens the road for detailed characterization of the ligand structure and even of the influence of the important bridging group in this class of compounds.

**XAES in the K-Edge Region and DFT Calculations.** In the following, we use K$\beta^{1,3}$ and K$\beta'$ detection to investigate site-selectivity in XAS spectra of **1**. The K$\beta^{2,5}$ calculations revealed significant delocalization of Fe-d electrons from both iron atoms of **1** in MOs with ligand character. For delocalization also of lower energy, i.e. 3p electrons and localized 1s holes, site-selectivity may be flawed because the emission in the whole K$\beta^{1,3}$ region would contain similar contributions from both iron sites. The energies of the 1s- and 3p-levels of **1** from DFT argue against such a scenario. Rather, localized Fe-3p orbitals are obtained, and furthermore, the Fe1−3p to Fe1−1s and Fe1−3p to Fe2−1s energy differences are similar but at least about 1 eV lower than the Fe2−3p to Fe1−1s and Fe2−3p to Fe2−1s energy differences (Table 3). Accordingly, by measuring the XAS spectra of **1** for low or high detection energies in the K$\beta^{1,3}$ line region, preferentially transitions from 3p-levels of Fe1 or Fe2 should be probed.

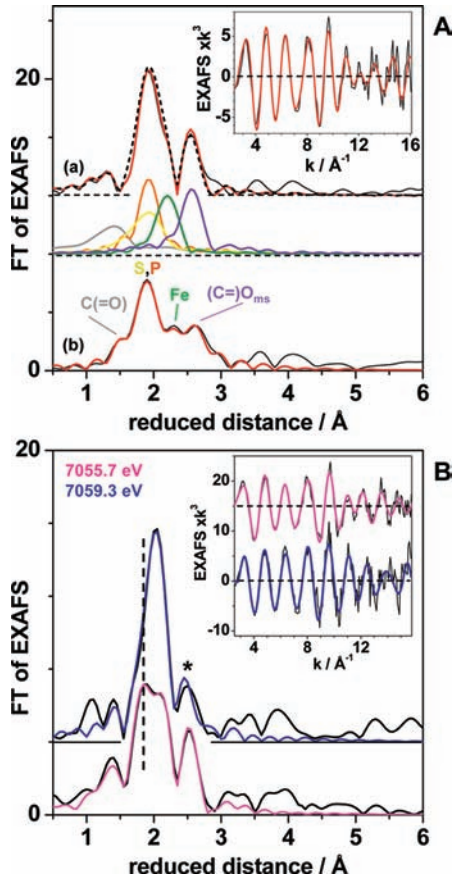


**Figure 10.** EXAFS analysis of complex **1**. (A) Fourier-transform (FT) of the K$\alpha$-fluorescence detected EXAFS spectrum (a) in the inset (black lines, experimental data; red lines, simulations with parameters in Table 4A; the dashed line shows a simulation with the 4-shell model in Table 4A); the contributions of the individual iron-backscatterer interactions are shown as colored lines below (ms, multiple-scattering contribution). The FT was calculated for *k*-values of 1.6−16.2 Å$^{-1}$ and using cos$^2$ windows extending over 10% at both *k*-range ends. The FT spectrum (b) was calculated from the same EXAFS spectrum in the inset, but using a *k*-range of 4.4−16.2 Å$^{-1}$ and cos$^2$ windows over 15% and 5% at low and high *k*-range ends (black line, experimental data; red line, simulation with the same parameters as used for spectrum a). (B) FTs of EXAFS spectra (in the inset) measured for two K$\beta^{1,3}$ detection energies (±0.5 eV). Spectra are vertically shifted for comparison. Black lines, experimental data; colored lines, simulations with parameters in Table 4B. Vertical dashes mark FT features comprising Fe−C(=O) contributions; the asterisk denotes the Fe(—C)=$O_{ms}$ peak. FTs were calculated for *k*-values of 1.6−15.8 Å$^{-1}$ with cos$^2$ windows over 10% of the *k*-range ends.

*Apparent Site-Selectivity in the XANES.* The conventional total-fluorescence detected XANES spectrum of **1** reveals a well discernible pre-edge feature around 7113 eV with two apparent peaks, a shoulder at ∼7120 eV in the main edge rise, and a moderate amplitude of the primary edge maximum at ∼7127 eV (Figure 7A). Notably, the XANES spectra of **1** derived from total-fluorescence (K$\alpha$ + K$\beta$), partial K$\beta$ fluorescence (K$\beta'$ + K$\beta^{1,3}$), or transmission detection were virtually identical (Supporting Information Figure S2). The pre-edge feature commonly is attributed to dipole-forbidden 1s → 3d transitions gaining intensity by the admixture of metal-p and ligand-s,p character into the 3d levels.[107] For $FeS_2$ it shows only a single peak, due to the low-spin 3d($t_{2g}^6e_g^0$) configuration of $O_h$ Fe(II).[108] The first pre-edge feature in **1** ($Fe^I_2$) and


dx.doi.org/10.1021/ic2024154 | Inorg. Chem. 2012, 51, 4546−4559

**Table 4. EXAFS Simulation Parameters for Complex 1**[a]

| shell | $N_i$ (per Fe ion) | $R_i$ (Å) | $2\sigma^2_i$ x$10^3$ (Å$^2$) | $R_F$ (%) |
|---|---|---|---|---|
| (A) K$\alpha^{1,2}$-Fluorescence | | | | |
| Fe—C(=O) | 0.86 [1] | 1.73 [1.73] (1.73)[b] | 9 [15] | 8.6 [14.2] |
| Fe—C(=O) | 0.78 [1] | 1.83 [1.84] (1.83)[b] | 9 [12] | |
| Fe–P | 1.04 [1] | 2.25 [2.25] (2.23) | 2 [2] | |
| Fe–S | 2.01 [2] | 2.31 [2.31] (2.29) | 25 [20] | |
| Fe–Fe | 1.07 [1] | 2.51 [2.52] (2.53) | 8 [8] | |
| Fe(—C)=$O_{ms}$ | 1.64[c] [2] | 2.89 [2.88] (2.94) | 20 [6] | |
| C=O | 1.64[c] [2] | 1.24 [1.24] (1.16) | 0 [0] | |
| Fe–C(=O) | 1.58 [2] | 1.78 [1.79] (1.78) | 19 [20] | 8.9 [22.3] |
| Fe–S,P | 1.84 [3] | 2.24 [2.25] (2.26) | 6 [12] | |
| Fe–Fe | 1.04 [1] | 2.52 [2.52] (2.53) | 8 [11] | |
| Fe(—C)=$O_{ms}$ | 1.58[c] [2] | 2.88 [2.87] (2.94) | 19 [6] | |
| C=O | 1.58[c] [2] | 1.19 [1.18] (1.16) | 0 [0] | |
| (B) K$\beta^{1,3}$-Fluorescence, 7055.7 ± 0.5 eV | | | | |
| Fe–C(=O) | 2.28 [1.86] (3) | 1.80 [1.81] (1.79) | 8 [5] | 12.3 [13.8] |
| Fe–S,P | 1.96 [2.11] (2) | 2.25 [2.28] (2.29) | 9 [11] | |
| Fe–Fe | 1[d] [1[d]] (1) | 2.51 [2.51] (2.53) | 4 [5] | |
| Fe(—C)=$O_{ms}$ | 2.28[c] [1.86[c]] (3) | 2.87 [2.90] (2.95) | 12 [19] | |
| C=O | 2.28[c] [1.86[c]] (3) | 1.15 [1.15] (1.15) | 0 [0] | |
| (C) K$\beta^{1,3}$-Fluorescence, 7059.3 ± 0.5 eV | | | | |
| Fe–C(=O) | 0.88 [0.78] (1) | 1.82 [1.80] (1.73) | 2 [5] | 17.8 [19.9] |
| Fe–S,P | 3.51 [3.14] (4) | 2.29 [2.26] (2.26) | 12 [11] | |
| Fe–Fe | 1[d] [1[d]] (1) | 2.51 [2.51] (2.53) | 6 [5] | |
| Fe(—C)=$O_{ms}$ | 0.88[c] [0.78[c]] (1) | 2.90 [2.87] (2.92) | 25 [19] | |
| C=O | 0.88[c] [0.78[c]] (1) | 1.22 [1.16] (1.18) | 0 [0] | |

[a] $N_i$ is the coordination number, $R_i$ the interatomic distance, and $2\sigma^2_i$ the Debye–Waller factor. The C=O shell denotes the carbon–oxygen distance as derived in the fit approach including multiple-scattering (ms) contributions from the carbonyl ligands. (A) For the K$\alpha$-detected spectrum, two sets of parameters using 6- (top) or 4-shell (bottom) models are shown; values in brackets are for a fit with the integer coordination numbers from the crystal structure, and values in parentheses give the average of the respective crystallographic interatomic distances. (B) For the K$\beta^{1,3}$-detected spectra, fit results for the 4-shell approach are shown; values in brackets are for a fit with the same $2\sigma^2$-values used for both spectra, and the respective crystallographic values for Fe1 (top) and Fe2 (bottom) are given in parentheses. [b] Shortest and longest Fe–C(=O) bonds. [c] The *N*-values for $O_{ms}$ and C=O were restrained to the same value as (the sum of) *N*(Fe–C(=O)) in the fits. [d] *N*(Fe–Fe) was fixed to unity in the simulations. The EXAFS damping factor, $S_0^2$, was 0.85; the error sum, $R_F$,[81] was calculated for reduced distances of 1–3 Å of FT spectra (see Figure 10).

$Fe^0_2(CO)_9$ was at similar energies as that for $Fe^{II}S_2$. This suggests a similar energy difference between the Fe-1s and LUMO (mostly Fe-3d) electronic levels in these compounds, which apparently is not proportional to the formal iron valence. K-edge simulations using scattering theory[109] reproduced the main edge shapes and revealed that, in particular, the primary edge maximum, which is highest for $Fe_2(CO)_9$, is proportional to the number of CO ligands at iron (Figure 7A, inset). Accordingly, for **1** the calculated XANES spectrum of Fe1 with a higher number of CO ligands shows a much larger maximum compared to the spectrum of Fe2.

XANES spectra measured for low or high K$\beta^{1,3}$ detection energies and for the K$\beta'$ region are shown in Figure 7B. A larger primary edge maximum was observed for the lower K$\beta^{1,3}$ energy. Particularly interesting are changes in the pre-edge feature at the two K$\beta^{1,3}$ energies (Figure 7B, inset). For the low energy, a large first peak (at 7112.8 eV) and smaller second peak (at 7114.9 eV) were observed (peak area ratio of about 1.6:1), but for the high energy, the second peak was even larger than the first one (energies of 7113.2 and 7115.6 eV, area ratio of 0.9:1). The K$\beta'$-detected pre-edge was more similar to the spectrum measured for low K$\beta^{1,3}$ energies. Notably, for the more symmetric [FeFe] complexes **2**, $Fe_2S_2(CO)_6$, and $Fe_2(CO)_9$, the changes in the XANES spectra for detection at different K$\beta^{1,3}$ and K$\beta'$ energies were considerably less pronounced compared to the case of the asymmetric complex **1** (Supporting Information Figure S3). However, even for the completely symmetric complexes $Fe_2S_2(CO)_6$ and $Fe_2(CO)_9$, there are still noticeable spectral differences at different detection energies. This shows that the underlying electronic multiplet structure[107,110] also contributes to the spectral differences. At present it appears to us that, for the asymmetric complex **1**, the detection-energy dependent contributions from the two different iron sites to a significant extent are responsible for the spectral differences, whereas, for the symmetric complexes, multiplet structure may be dominant.

XANES spectra of **1** were measured using detection energies ranging over the whole K$\beta$ emission region. The largest edge maximum and smallest pre-edge peak ratio were observed at energies slightly below the K$\beta^{1,3}$ line center; the reverse behavior of parameters was observed at particularly high K$\beta^{1,3}$ energies and to a lesser extent for the lowest K$\beta^{1,3}$ energies (Figure 7C). According to the XANES calculations (Figure 7A) and to the DFT results described in the next section, these spectral changes seem to reflect a larger contribution of Fe1 at lower K$\beta^{1,3}$ energies and a larger contribution of Fe2 at high K$\beta^{1,3}$ energies. We thus attribute a significant part of the spectral changes to site selectivity in the XANES. This view is corroborated by the EXAFS results presented further down. Multiplet structure in the K$\beta$ emission spectra,[110] however, to some extent may also contribute to the spectral changes (see above and Supporting Information Figure S3). A fully quantitative description of the detection-energy dependent XANES spectra would require a quantitative calculation of the


dx.doi.org/10.1021/ic2024154 | *Inorg. Chem.* 2012, 51, 4546–4559

Kβ emission multiplet as well as of the site selective contributions, which is precluded at present.

*DFT Calculations of Pre-edge Transitions.* Excitations into MOs with Fe-d contributions that determine the pre-edge absorption were revealed by DFT calculations. In general, the calculated pre-edge spectra were in good agreement with the experiment and showed pronounced differences for Fe1 and Fe2 for the asymmetric complex **1** (Figure 8), but they were rather similar for the two iron atoms of the more symmetric complex **2** (Supporting Information Figure S3). The electronic transitions are of almost exclusive electric dipole character (>95% intensity); magnetic dipole and quadrupole contributions are negligible (<5%). For **1** and both Fe1 and Fe2, MOs with the dominant Fe-d($x^2 - y^2$) contribution are at the highest energy (Figure 8B). However, the MO with largest Fe-d($z^2$) character, which aligns with the bond to the apical iron ligands, is unoccupied and close to the Fe-d($x^2 - y^2$) level for Fe2, but at ∼3 eV lower energy and hence double occupied for Fe1. This nicely reflects the axial contraction at Fe1, due to the short (∼1.8 Å) apical CO bond and strong π-backbonding, lowering the Fe1-d($z^2$) energy, as opposed to the less covalent (∼2.2 Å) bond of the apical phosphorus group at Fe2. For the Fe1,2-d(*xy*,*xz*,*yz*) levels, the rather similar energies could not be clearly discriminated. One reason for this is the dependence of the calculated energies on the used DFT functional (BP86 or B3LYP). However, both functionals yielded similar overall MO structures (Figure 8C). We consider the energy differences for the BP86 and B3LYP functionals as an estimate of the uncertainty in the DFT calculated MO energies when compared to the experimentally determined values.[111,112]

The LUMO is dominated by Fe-d contributions, in particular, from Fe1-d($x^2 - y^2$), and thus, it is largely located at Fe1, independent of the used functional (Figure 8C). Assignment of the HOMO depended on the functional (MO dominated by Fe1-d($z^2$) for B3LYP or Fe2-d(*yz*) for BP86), as well as the HOMO−LUMO energy gap (3.65 eV for B3LYP, 1.86 eV for BP86). The mean value of 2.8 ± 0.9 eV is in agreement with the experimental value of ∼2.8 eV (see above). In summary, for Fe1 the configuration of MOs with the largest Fe-d contributions, to some extent, resembles the atomic level picture of a $C_{4v}$ ion with Fe(0) ($d^8$) character, whereas for Fe2 the MO configuration is more similar to an $O_h$ ion with low-spin Fe(II) ($d^6$) character (Supporting Information Figure S4). The more symmetric axial coordination with an Fe−P bond (∼2.2 Å) and a putative Fe−Fe bond (∼2.5 Å)[113] for Fe2, and the axial contraction due to the short Fe−CO bond (∼1.8 Å) for Fe1, could explain the different d-level degeneracy. It should be noted that Mulliken population analysis yielded total Fe-d AO occupancies of ∼7 (i.e., $d^7$) for both iron atoms and an Fe-d($z^2$) occupancy for Fe1, which was only ∼0.1 $e^-$ higher than that for Fe2 (Supporting Information Table S1). The MO picture clearly describes the electronic structure of **1** and associated X-ray spectral features more adequately. The DFT calculations furthermore reveal that only the first pre-edge peak can be considered as a true 1s → 3d feature, because it reflects excitations into two Fe-d dominated MOs, whereas the second peak is rather a low-lying edge transition of various MOs with mostly C-p character (Figure 8A).

*Spin-Selective XAES.* For high-spin Fe(III) in, for example, $Fe_3O_4$,[48] the Kβ$^{1,3}$-detected XANES reveals a pronounced pre-edge peak, which is absent for Kβ′-detection (Figure 2E). In other words, Kβ′ fluorescence emission is observed for nonresonant excitation but missing for excitation into 3d resonances (Figure 2D). This is explained by the absence of a spin-up 3p hole in the final state probing unpaired spin-up 3d electrons in the latter case (Figure 4). For complex **1**, rather the opposite behavior was observed (Figure 9). The Kβ′-detected pre-edge peak is even larger compared to Kβ$^{1,3}$-detection (Figure 7B), and Kβ′ emission is almost absent for nonresonant excitation and pronounced for resonant excitation (Figure 3A). In the case of **1**, the unpaired 3d spin is created only upon excitation of a 1s electron into the 3d levels. This spectral behavior thus is further evidence that the Kβ′ emission mostly is explained by 3p,3d spin-up/down interactions because both final state configurations are expected after resonant excitation of complex **1** (Figure 9). Kβ resonant inelastic X-ray scattering (RIXS),[114,115] therefore, is particularly promising for probing the 3d level configuration of low-spin [FeFe] complexes, for example in different redox states.

*Site-Selective EXAFS Experiments.* EXAFS analysis of **1** was performed to study site-selectivity. The conventional Kα-fluorescence detected EXAFS spectrum of **1** is shown in Figure 10A. The Fourier-transform (FT) calculated over the whole available *k*-range of data (1.6−16.2 $Å^{-1}$) reveals three main features, which are attributable to Fe—C(═O) and Fe—S,P,Fe interactions and to a prominent multiple-scattering (ms) contribution, due to the almost linear Fe—C═O arrangement in the structure.[116−119] Calculating the FT starting from higher *k*-values unmasked the Fe−Fe distance as a separate peak (Figure 10A). A good spectral simulation was achieved by using the coordination numbers (*N*) and similar interatomic distances (*R*), for example an Fe−Fe distance of 2.52 Å, as in the crystal structure of **1**[67] (Figure 10A, Table 4A). Using a six-shell model, even estimation of the longest and shortest Fe—C(═O) bonds (∼1.73 Å and ∼1.83 Å) and discrimination between the longer Fe—S and shorter Fe—P bonds was feasible. Overall, the interatomic distances were slightly shorter in the EXAFS model, likely due to the lower temperature (20 K) during X-ray spectroscopy,[120] but the overall geometry of **1** in the powder material presumably closely resembles its structure in single crystals.[67]

EXAFS spectra as measured for low and high energy Kβ$^{1,3}$ emission detection (7055.7 ± 0.5 eV and 7059.3 ± 0.5 eV) are shown in Figure 10B. Visual inspection of the FT spectra revealed larger Fe−C(═O) and Fe(−C)═$O_{ms}$ FT peaks in the low-energy spectrum and a larger main FT peak in the high-energy spectrum, indicating different structural contributions to the two spectra. EXAFS simulations were done using a simplified model with four Fe-backscatterer shells, which also provided a reasonable simulation of the Kα-detected spectrum (Figure 10A, Table 4A). The simulation parameters revealed an about twice as large number of Fe−CO interactions and an about halved number of Fe−S,P bonds per iron atom for the low energy EXAFS compared to the high energy spectrum (Table 4B). We note that EXAFS coordination numbers (*N*) in the fit are statistically coupled to the Debye−Waller parameter ($2\sigma^2$) so that an *N*-error of 10−20% may be anticipated. However, using the same $2\sigma^2$ values in the simulations of both spectra resulted in relatively small changes (<20%) in the coordination numbers of the Fe−CO and Fe−S,P bonds determined from the low and high energy spectra (Table 4B, values in brackets). These results suggest that the two different iron sites are quite selectively probed by the two Kβ$^{1,3}$-detected EXAFS spectra of **1**. This notion was further corroborated by the EXAFS data of complex **2**, which were quite similar for low


dx.doi.org/10.1021/ic2024154 | *Inorg. Chem.* 2012, 51, 4546−4559

and high $K\beta^{1,3}$-detection energies, as expected for its two overall similar iron sites (Supporting Information Figure S5).

Compared to the structure of **1** showing Fe1/Fe2 ratios of 3:1 for the Fe-CO bonds and 0.5:1 for the Fe−S,P bonds, the experimental ratios were diminished to about 2.6:1 and 0.6:1. However, as discussed above, absolute site-selectivity cannot be expected, due to multiplet structure and the contribution of Fe1,Fe2−3p → Fe2,Fe1−1s crossover transitions in the $K\beta^{1,3}$ emission (compare Figure 6). These effects and/or the absence of crystal packing effects,[121] a lower temperature in the EXAFS measurements,[30] and X-ray Raman scattering contributions[35,48] might also account for the slight deviations of the metal−ligand distances for the two iron sites in the K$\beta$-EXAFS analysis compared to the crystal structure (Table 4B). Mathematical procedures for deconvolution of site-selective EXAFS spectra to yield the pure spectra of the individual sites have been described by other authors,[47] but this has not been attempted here because of the uncertainties discussed above. In any event, the EXAFS results on **1** suggest that site-selective XAES experiments seem to be feasible also for [FeFe] molecules with tightly connected metal ions and partially delocalized electronic structure.

## CONCLUSIONS

For an asymmetrically ligated diiron complex we have shown that information on the individual iron atoms with respect to their electronic configuration (effective spin and oxidation states, HOMO−LUMO energy gap, d-orbital structure) and molecular geometry (chemical nature of ligands, bond lengths, coordination numbers) can be obtained by the application of high-resolution X-ray absorption spectroscopy with narrow-band K$\beta$ fluorescence detection (XAES). Apparent correlations between the K$\beta$ emission energy and intensity on the one hand and the ligand field strength and bond length on the other hand were found for a variety of low-spin iron compounds. The K$\beta$ valence-to-core transitions ($K\beta^{2,5}$) bear particularly selective information on the coordination environment, thereby enabling, for example, approximate ligand counting. Calculation results by DFT methods for $K\beta^{2,5}$ emission lines and low-lying transitions (e.g., 1s → 3d) in the XANES of [FeFe] models are in good agreement with the experimental data, which extends and confirms previous studies[66,106] and facilitates quantitative interpretation of XAS and XES spectra. These results suggest that even relatively subtle chemical changes in the complexes, i.e. due to metal-hydride bond formation or protonation at the bridging ligand, are expected to be accessible in XAES data. In conclusion, XAES is a powerful tool for investigating the specific structure of individual metal sites in binuclear iron compounds and to verify and interpret the desired effects of built-in chemical variations. Site- and spin-selectivity may be obtained, as long as sufficient asymmetry is present in the metal coordination spheres. Further experiments to apply these methods to the active-site H-cluster in [FeFe] hydrogenase proteins and tailored models under reaction conditions, i.e. in solution, are underway in our laboratories.

## ASSOCIATED CONTENT

### Supporting Information

(1) Crystal structures of the iron compounds (Figure S1), (2) Fe-d atomic orbital occupancies in complex **1** from DFT (Table S1), and (3) further XAES data of **1** and reference compounds (Figures S2, S3, S4, and S5; Table S2). This material is available free of charge via the Internet at http://pubs.acs.org.

## AUTHOR INFORMATION

### Corresponding Author

*Address: Freie Universität Berlin, FB Physik, Arnimallee 14, 14195 Berlin, Germany. Phone: +49 30 838 56101. Fax: +49 30 838 56299. E-mail: michael.haumann@fu-berlin.de.

### Notes

The authors declare no competing financial interest.

## ACKNOWLEDGMENTS

Financial support from the Deutsche Forschungsgemeinschaft (DFG; Grant Ha3265/3-1 and funding within the Unicat Cluster of Excellence Berlin to M.H.); from the Swedish Research Council, the Knut and Alice Wallenberg Foundation, and the Swedish Energy Agency (to S.O.); and from the European Union (FP7, Energy 212508, SOLAR-H2 consortium) is gratefully acknowledged. K.G.V.H. thanks "Stiftelsen Bengt Lundqvist minne" and the Wenner-Gren Foundation for fellowships. M.H. thanks the DFG for a Heisenberg fellowship. We thank Drs. T.-C. Weng and P. Glatzel at ID26 of ESRF for excellent support and valuable discussions, and Dr. I. Zaharieva (FU-Berlin) for critical reading of the manuscript.

## REFERENCES

(1) *Committee on Climate Change: The Renewable Energy Review*; U.K., 2011, available at http://www.theccc.org.uk/reports/renewable-energy-review.
(2) Lubitz, W.; Reijerse, E. J.; Messinger, J. *Energy Environ. Sci.* **2008**, *1*, 15−31.
(3) Nocera, D. G. *Inorg. Chem.* **2009**, *48*, 10001−10017.
(4) Hammarström, L.; Winkler, J. R.; Gray, H. B.; Styring, S. *Science* **2011**, *333*, 288.
(5) Gust, D.; Moore, T. A.; Moore, A. L. *Acc. Chem. Res.* **2009**, *42*, 1890−1898.
(6) Magnuson, A.; Anderlund, M.; Johansson, O.; Lindblad, P.; Lomoth, R.; Polivka, T.; Ott, S.; Stensjö, K.; Styring, S.; Sundström, V.; Hammarström, L. *Acc. Chem. Res.* **2009**, *42*, 1899−1909.
(7) Krassen, H.; Ott, S.; Heberle, J. *Phys. Chem. Chem. Phys.* **2011**, *13*, 47−57.
(8) Dau, H.; Haumann, M. *Coord. Chem. Rev.* **2008**, *252*, 273−295.
(9) Dau, H.; Limberg, C.; Reier, T.; Risch, M.; Roggan, S.; Strasser, P. *ChemCatChem* **2010**, *2*, 724−761.
(10) McEvoy, J. P.; Brudvig, G. W. *Chem. Rev.* **2006**, *106*, 4455−4483.
(11) Mulder, D. W.; Shepard, E. M.; Meuser, J. E.; Joshi, N.; King, P. W.; Posewitz, M. C.; Broderick, J. B.; Peters, J. W. *Structure* **2011**, *19*, 1038−1052.
(12) Stripp, S. T.; Happe, T. *Dalton Trans.* **2009**, 9960−9969.
(13) Fontecilla-Camps, J. C.; Volbeda, A.; Cavazza, C.; Nicolet, Y. *Chem. Rev.* **2007**, *107*, 4273−4303.
(14) Shima, S.; Pilak, O.; Vogt, S.; Schick, M.; Stagni, M. S.; Meyer-Klaucke, W.; Warkentin, E.; Thauer, R. K.; Ermler, U. *Science* **2008**, *321*, 572−575.
(15) Rauchfuss, T. B. *Science* **2007**, *316*, 553−554.
(16) Armstrong, F. A.; Fontecilla-Camps, J. C. *Science* **2008**, *321*, 498−499.
(17) Tard, C.; Pickett, C. J. *Chem. Rev.* **2009**, *109*, 2245−2274.
(18) Gloaguen, F.; Rauchfuss, T. B. *Chem. Soc. Rev.* **2009**, *38*, 100−108.
(19) Artero, V.; Fontecave, M. *Coord. Chem. Rev.* **2005**, *249*, 1518−1535.
(20) Darensbourg, M. Y. *Comments Inorg. Chem.* **2010**, *31*, 144−152.
(21) Erdem, O. F.; Schwartz, L.; Stein, M.; Silakov, A.; Kaur-Ghumaan, S.; Huang, P.; Ott, S.; Reijerse, E. J.; Lubitz, W. *Angew. Chem., Int. Ed. Engl.* **2011**, *50*, 1439−1443.
(22) Darensbourg, M. Y. *Nature* **2005**, *433*, 589−591.

(23) Lomoth, R.; Kaur-Ghumaan, S.; Schwartz, L.; Stein, M.; Ott, S. *Angew. Chem., Int. Ed. Engl.* **2010**, *49*, 8033−8036.
(24) Tard, C.; Liu, X.; Ibrahim, S. K.; Bruschi, M.; De Gioia, L.; Davies, S. C.; Yang, X.; Wang, L. S.; Sawers, G.; Pickett, C. J. *Nature* **2005**, *433*, 610−613.
(25) Peters, J. W.; Lanzilotta, W. N.; Lemon, B. J.; Seefeldt, L. C. *Science* **1998**, *282*, 1853−1858.
(26) Nicolet, Y.; Lemon, B. J.; Fontecilla-Camps, J. C.; Peters, J. W. *Trends Biochem. Sci.* **2000**, *25*, 138−143.
(27) Song, L. C.; Xie, Z. J.; Liu, X. F.; Ming, J. B.; Ge, J. H.; Zhang, X. G.; Yan, T. Y.; Gao, P. *Dalton Trans.* **2011**, *40*, 837−846.
(28) Felton, G. A. N.; Mebi, C. A.; Petro, B. J.; Vannucci, A. K.; Evans, D. H.; Glass, R. S.; Lichtenberger, D. L. *J. Organomet. Chem.* **2009**, *694*, 2681−2699.
(29) Wright, J. A.; Webster, L.; Jablonskyte, A.; Woi, P. M.; Ibrahim, S. K.; Pickett, C. J. *Faraday Discuss.* **2011**, *148*, 359−371.
(30) Löscher, S.; Schwartz, L.; Stein, M.; Ott, S.; Haumann, M. *Inorg. Chem.* **2007**, *46*, 11094−11105.
(31) Singh, P. S.; Rudbeck, H. C.; Huang, P.; Ezzaher, S.; Eriksson, L.; Stein, M.; Ott, S.; Lomoth, R. *Inorg. Chem.* **2009**, *48*, 10883−10885.
(32) Singh, J.; Lamberti, C.; van Bokhoven, J. A. *Chem. Soc. Rev.* **2010**, *39*, 4754−4766.
(33) Pushkar, Y.; Long, X.; Glatzel, P.; Brudvig, G. W.; Dismukes, G. C.; Collins, T. J.; Yachandra, V. K.; Yano, J.; Bergmann, U. *Angew. Chem., Int. Ed. Engl.* **2010**, *49*, 800−803.
(34) Messinger, J.; Robblee, J. H.; Bergmann, U.; Fernandez, C.; Glatzel, P.; Visser, H.; Cinco, R. M.; McFarlane, K. L.; Bellacchio, E.; Pizarro, S. A.; Cramer, S. P.; Sauer, K.; Klein, M. P.; Yachandra, V. K. *J. Am. Chem. Soc.* **2001**, *123*, 7804−7820.
(35) Bergmann, U.; Glatzel, P.; Robblee, J. H.; Messinger, J.; Fernandez, C.; Cinco, R.; Visser, H.; McFarlane, K.; Bellacchio, E.; Pizarro, S.; Sauer, K.; Yachandra, V. K.; Klein, M. P.; Cox, B. L.; Nealson, K. H.; Cramer, S. P. *J. Synchrotron Radiat.* **2001**, *8*, 199−203.
(36) Visser, H.; Anxolabehere-Mallart, E.; Bergmann, U.; Glatzel, P.; Robblee, J. H.; Cramer, S. P.; Girerd, J.-J.; Sauer, K.; Klein, M. P.; Yachandra, V. K. *J. Am. Chem. Soc.* **2001**, *123*, 7031−7039.
(37) Mijovilovich, A.; Hamman, S.; Thomas, F.; de Groot, F. M.; Weckhuysen, B. M. *Phys. Chem. Chem. Phys.* **2011**, *13*, 5600−5604.
(38) Haumann, M.; Liebisch, P.; Müller, C.; Barra, M.; Grabolle, M.; Dau, H. *Science* **2005**, *310*, 1019−1021.
(39) Strange, R. W.; Feiters, M. C. *Curr. Opin. Struct. Biol.* **2008**, *18*, 609−616.
(40) Glatzel, P.; Bergmann, U. *Coord. Chem. Rev.* **2005**, *249*, 65−95.
(41) De Groot, F.; Kotani, A. *Core Level Spectroscopy of Solids*; Taylor & Francis and CRC Press: Boca Raton, FL, USA, 2008.
(42) Namatame, H.; Fujimori, A.; Takagi, H.; Uchida, S.; de Groot, F. M.; Fuggle, J. C. *Phys. Rev. B: Condens. Matter* **1993**, *48*, 16917−16925.
(43) Abbate, M.; Fuggle, J. C.; Fujimori, A.; Tjeng, L. H.; Chen, C. T.; Potze, R.; Sawatzky, G. A.; Eisaki, H.; Uchida, S. *Phys. Rev. B: Condens. Matter* **1993**, *47*, 16124−16130.
(44) Grioni, M.; van Acker, J. F.; Czyzyk, M. T.; Fuggle, J. C. *Phys. Rev. B: Condens. Matter* **1992**, *45*, 3309−3318.
(45) Weijs, P. J.; van Leuken, H.; de Groot, R. A.; Fuggle, J. C.; Reiter, S.; Wiech, G.; Buschow, K. H. *Phys. Rev. B: Condens. Matter* **1991**, *44*, 8195−8203.
(46) de Groot, F. M.; Fuggle, J. C.; Thole, B. T.; Sawatzky, G. A. *Phys. Rev. B: Condens. Matter* **1990**, *42*, 5459−5468.
(47) Glatzel, P.; Jacquamet, L.; Bergmann, U.; de Groot, F. M. F.; Cramer, S. P. *Inorg. Chem.* **2002**, *41*, 3121−3127.
(48) Yamaoka, H.; Oura, M.; Taguchi, M.; Morikawa, T.; Takahiro, K.; Terai, A.; Kawatsura, K.; Vlaicu, A. M.; Ito, Y.; Mukoyama, T. *J. Phys. Soc. Jpn.* **2004**, *73*, 3182−3191.
(49) Badro, J.; Struzhkin, V. V.; Shu, J. F.; Hemley, R. J.; Mao, H. K.; Kao, C. C.; Rueff, J. P.; Shen, G. Y. *Phys. Rev. Lett.* **1999**, *83*, 4101−4104.
(50) De Groot, F. M. F.; Fontaine, A.; Kao, C. C.; Krisch, M. *J. Phys.: Condens. Matter* **1994**, *6*, 6875−6884.
(51) Peng, G.; Wang, X.; Randall, C. R.; Moore, J. A.; Cramer, S. P. *Appl. Phys. Lett.* **1994**, *65*, 2527−2529.
(52) Peng, G.; De Groot, F. M. F.; Hamalainen, K.; Moore, J. A.; Wang, X.; Grush, M. M.; Hastings, J. B.; Siddons, D. P.; Armstrong, W. H.; Mullins, O. C.; Cramer, S. P. *J. Am. Chem. Soc.* **1994**, *116*, 2914−2920.
(53) Zaharieva, I.; Chernev, P.; Risch, M.; Gerencser, L.; Berggren, G.; Shevchenko, G.; Anderlund, M.; Weng, T.-C.; Haumann, M.; Dau, H. *J. Phys. Conf. Ser.* **2009**, *190*, 012142, 012141−012146.
(54) Darensbourg, M. Y.; Lyon, E. J.; Smee, J. J. *Coord. Chem. Rev.* **2000**, *206*, 533−561.
(55) Schünemann, V.; Winkler, H. *Rep. Prog. Phys.* **2000**, *63*, 263−353.
(56) Razavet, M.; Davies, S. C.; Hughes, D. L.; Barclay, J. E.; Evans, D. J.; Fairhurst, S. A.; Liu, X. M.; Pickett, C. J. *Dalton Trans.* **2003**, 586−595.
(57) Justice, A. K.; Rauchfuss, T. B.; Wilson, S. R. *Angew. Chem., Int. Ed. Engl.* **2007**, *46*, 6152−6154.
(58) Song, L. C.; Yang, Z. Y.; Bian, H. Z.; Hu, Q. M. *Organometallics* **2004**, *23*, 3082−3084.
(59) Horikawa, Y.; Tokushima, T.; Harada, Y.; Takahashi, O.; Chainani, A.; Senba, Y.; Ohashi, H.; Hiraya, A.; Shin, S. *Phys. Chem. Chem. Phys.* **2009**, *11*, 8676−8679.
(60) Tokushima, T.; Horikawa, Y.; Harada, Y.; Takahashi, O.; Hiraya, A.; Shin, S. *Phys. Chem. Chem. Phys.* **2009**, *11*, 1679−1682.
(61) Izumi, Y.; Nagamori, H.; Kiyotaki, F.; Minato, T. *J. Synchrotron Radiat.* **2001**, *8*, 605−607.
(62) Buser, H. J.; Schwarzenbach, D.; Petter, W.; Ludi, A. *Inorg. Chem.* **1977**, *16*, 2704−2710.
(63) Smolentsev, G.; Soldatov, A. V.; Messinger, J.; Merz, K.; Weyhermüller, T.; Bergmann, U.; Pushkar, Y.; Yano, J.; Yachandra, V. K.; Glatzel, P. *J. Am. Chem. Soc.* **2009**, *131*, 13161−13167.
(64) Gerth, C.; Tiedtke, K.; Martins, M.; Obst, B.; Zimmermann, P.; Glatzel, P.; Verweyen, A.; Wernet, P.; Sonntag, B. *J. Phys. B* **1998**, *31*, 2539−2547.
(65) Cramer, S. P.; Bergmann, U.; Horne, C. R.; Collins, T. J.; Workman, J. M. *Chem. Phys. Lett.* **1999**, *302*, 119−124.
(66) Lee, N.; Petrenko, T.; Bergmann, U.; Neese, F.; DeBeer, S. *J. Am. Chem. Soc.* **2010**, *132*, 9715−9727.
(67) Ezzaher, S.; Gogoll, A.; Bruhn, C.; Ott, S. *Chem. Commun.* **2010**, *46*, 5775−5777.
(68) Gloaguen, F.; Lawrence, J. D.; Rauchfuss, T. B.; Benard, M.; Rohmer, M. M. *Inorg. Chem.* **2002**, *41*, 6573−6582.
(69) Zhao, X.; Hsiao, Y. M.; Lai, C. H.; Reibenspies, J. H.; Darensbourg, M. Y. *Inorg. Chem.* **2002**, *41*, 699−708.
(70) Ezzaher, S.; Capon, J. F.; Gloaguen, F.; Petillon, F. Y.; Schollhammer, P.; Talarmin, J.; Pichon, R.; Kervarec, N. *Inorg. Chem.* **2007**, *46*, 3426−3428.
(71) Silakov, A.; Wenk, B.; Reijerse, E.; Lubitz, W. *Phys. Chem. Chem. Phys.* **2009**, *11*, 6592−6599.
(72) Ryde, U.; Greco, C.; De Gioia, L. *J. Am. Chem. Soc.* **2010**, *132*, 4512−4513.
(73) Pachter, R.; Hong, G.; Cornish, A. J.; Hegg, E. L. *Biochim. Biophys. Acta* **2011**, *1807*, 510−517.
(74) De Gioia, L.; Zampella, G.; Fantucci, P. *Chem. Commun.* **2010**, *46*, 8824−8826.
(75) Barton, B. E.; Rauchfuss, T. B. *Inorg. Chem.* **2008**, *47*, 2261−2263.
(76) Jousselme, B.; Tran, P. D.; Le Goff, A.; Heidkamp, J.; Guillet, N.; Palacin, S.; Dau, H.; Fontecave, M.; Artero, V. *Angew. Chem., Int.. Ed.* **2011**, *50*, 1371−1374.
(77) Bullock, R. M.; Helm, M. L.; Stewart, M. P.; DuBois, M. R.; DuBois, D. L. *Science* **2011**, *333*, 863−866.
(78) Eremenko, I. L.; Berke, H.; Vanderzeijden, A. A. H.; Kolobkov, B. I.; Novotortsev, V. M. *J. Organomet. Chem.* **1994**, *471*, 123−132.
(79) Schwartz, L.; Eilers, G.; Eriksson, L.; Gogoll, A.; Lomoth, R.; Ott, S. *Chem. Commun. (Cambridge)* **2006**, 520−522.
(80) Wei, C. H.; Dahl, L. F. *Inorg. Chem.* **1965**, *4*, 1−&.

(81) Dau, H.; Liebisch, P.; Haumann, M. *Anal. Bioanal. Chem.* **2003**, *376*, 562−583.
(82) Löscher, S.; Zebger, I.; Andersen, L. K.; Hildebrandt, P.; Meyer-Klaucke, W.; Haumann, M. *FEBS Lett.* **2005**, *579*, 4287−4291.
(83) Zabinsky, S. I.; Rehr, J. J.; Ankudinov, A. L.; Albers, R. C.; Eller, M. J. *Phys. Rev. B* **1995**, *52*, 2995−3009.
(84) Neese, F. Orca: An ab-initio, DFT, and semiempirical electronic structure package. V.2.6.35; Theoretical chemistry group, University of Bonn: Bonn, Germany, 2008.
(85) Becke, A. D. *Phys. Rev. A* **1988**, *38*, 3098.
(86) Perdew, J. P. *Phys. Rev. B* **1986**, *33*, 8822.
(87) Kim, K.; Jordan, K. D. *J. Phys. Chem.* **1994**, *98*, 10089−10094.
(88) Schäfer, A.; Huber, C.; Ahlrichs, R. *J. Chem. Phys.* **1994**, *100*, 5829−5835.
(89) Mulliken, R. S. *J. Chem. Phys.* **1955**, *23*, 1833−1840.
(90) DeBeer George, S.; Petrenko, T.; Neese, F. *J. Phys. Chem. A* **2008**, *112*, 12936−12943.
(91) Glatzel, P.; Bergmann, U.; de Groot, F. M. F.; Cramer, S. P. *Phys. Rev. B* 2001, *64*.
(92) Hamalainen, K.; Kao, C. C.; Hastings, J. B.; Siddons, D. P.; Berman, L. E.; Stojanoff, V.; Cramer, S. P. *Phys. Rev. B* **1992**, *46*, 14274−14277.
(93) Tsutsumi, K.; Nakamori, H.; Ichikawa, K. *Phys. Rev. B* **1976**, *13*, 929−933.
(94) Sakurai, K.; Eba, H.; Numako, C.; Iihara, J. *Anal. Chem.* **2000**, *72*, 2613−2617.
(95) Fujimori, A.; Mamiya, K.; Mizokawa, T.; Miyadai, T.; Sekiguchi, T.; Takahashi, H.; Mori, N.; Suga, S. *Phys. Rev. B* **1996**, *54*, 16329−16332.
(96) Schönherr, T. *Optical Spectra and Chemical Bonding in Inorganic Compounds*; Springer: New York, 2004; Vols. *I* and *II*.
(97) Jörgensen, C. K. *Discuss. Faraday Soc.* **1958**, *26*, 110−115.
(98) Ishii, T.; Tsuboi, S.; Sakane, G.; Yamashita, M.; Breedlove, B. K. *Dalton Trans.* **2009**, 680−687.
(99) Lever, A. B. P. In *Werner Centennial*; Kauffman, G. B., Ed.; ACS Publications: Washington, USA, 1967; pp 430−451.
(100) Trueba, A.; Garcia-Fernandez, P.; Garcia-Lastra, J. M.; Aramburu, J. A.; Barriuso, M. T.; Moreno, M. *J. Phys. Chem. A* 2011.
(101) Brunold, T. C.; Fiedler, A. T. *Inorg. Chem.* **2005**, *44*, 1794−1809.
(102) Ellgen, P. C.; Gerlach, J. N. *Inorg. Chem.* **1973**, *12*, 2526−2532.
(103) Roy, L. E.; Batista, E. R.; Hay, P. J. *Inorg. Chem.* **2008**, *47*, 9228−9237.
(104) Gloaguen, F.; Lawrence, J. D.; Schmidt, M.; Wilson, S. R.; Rauchfuss, T. B. *J. Am. Chem. Soc.* **2001**, *123*, 12518−12527.
(105) Eilers, G.; Schwartz, L.; Stein, M.; Zampella, G.; de Gioia, L.; Ott, S.; Lomoth, R. *Chem.—Eur. J.* **2007**, *13*, 7075−7084.
(106) DeBeer, S.; Beckwith, M. A.; Roemelt, M.; Collomb, M. N.; DuBoc, C.; Weng, T. C.; Bergmann, U.; Glatzel, P.; Neese, F. *Inorg. Chem.* **2011**, *50*, 8397−8409.
(107) Westre, T. E.; Kennepohl, P.; DeWitt, J. G.; Hedman, B.; Hodgson, K. O.; Solomon, E. I. *J. Am. Chem. Soc.* **1997**, *119*, 6297−6314.
(108) Stevens, E. D.; Delucia, M. L.; Coppens, P. *Inorg. Chem.* **1980**, *19*, 813−820.
(109) Ankudinov, A. L.; Ravel, B.; Rehr, J. J.; Conradson, S. D. *Phys. Rev. B* **1998**, *58*, 7565−7576.
(110) Wang, X.; Randall, C. R.; Peng, G.; Cramer, S. P. *Chem. Phys. Lett.* **1995**, *243*, 469−473.
(111) George, S. D.; Petrenko, T.; Neese, F. *J. Phys. Chem. A* **2008**, *112*, 12936−12943.
(112) Chandrasekaran, P.; Stieber, S. C. E.; Collins, T. J.; Que, L.; Neese, F.; DeBeer, S. *Dalton Trans.* **2011**, *40*, 11070−11079.
(113) Pauling, L. *Proc. Natl. Acad. Sci. U.S.A.* **1976**, *73*, 4290−4293.
(114) Bauer, M.; Gastl, C. *Phys. Chem. Chem. Phys.* **2010**, *12*, 5575−5584.
(115) de Groot, F. M.; Glatzel, P.; Bergmann, U.; van Aken, P. A.; Barrea, R. A.; Klemme, S.; Havecker, M.; Knop-Gericke, A.; Heijboer, W. M.; Weckhuysen, B. M. *J. Phys. Chem. B* **2005**, *109*, 20751−20762.
(116) Czech, I.; Stripp, S.; Sanganas, O.; Leidel, N.; Happe, T.; Haumann, M. *FEBS Lett.* **2011**, *585*, 225−230.
(117) Stripp, S.; Sanganas, O.; Happe, T.; Haumann, M. *Biochemistry* **2009**, *48*, 5042−5049.
(118) Prestipino, C.; Capello, L.; D'Acapito, F.; Lamberti, C. *Phys. Chem. Chem. Phys.* **2005**, *7*, 1743−1746.
(119) Wittayakun, J.; Khabuanchalad, S.; Lobo-Lapidus, R. J.; Stoll, S.; Britt, R. D.; Gates, B. C. *J. Phys. Chem. C* **2010**, *114*, 17212−17221.
(120) Havelius, K. G.; Reschke, S.; Horn, S.; Doring, A.; Niks, D.; Hille, R.; Schulzke, C.; Leimkühler, S.; Haumann, M. *Inorg. Chem.* **2011**, *50*, 741−748.
(121) Si, G.; Wang, W. G.; Wang, H. Y.; Tung, C. H.; Wu, L. Z. *Inorg. Chem.* **2008**, *47*, 8101−8111.
(122) Fiddy, J. M.; Hall, I.; Grandjean, F.; Long, G. J.; Russo, U. *J. Phys.: Condens. Matter* **1990**, *2*, 10091−10107.
(123) Stripp, S. T.; Goldet, G.; Brandmayr, C.; Sanganas, O.; Vincent, K. A.; Haumann, M.; Armstrong, F. A.; Happe, T. *Proc. Natl. Acad. Sci. U. S. A.* **2009**, *106*, 17331−17336.
(124) Nicolet, Y.; de Lacey, A. L.; Vernede, X.; Fernandez, V. M.; Hatchikian, E. C.; Fontecilla-Camps, J. C. *J. Am. Chem. Soc.* **2001**, *123*, 1596−1601.
(125) Lubitz, W.; Reijerse, E.; van Gastel, M. *Chem. Rev.* **2007**, *107*, 4331−4365.
(126) Silakov, A.; Kamp, C.; Reijerse, E.; Happe, T.; Lubitz, W. *Biochemistry* **2009**, *48*, 7780−7786.
(127) Cotton, F. A.; Troup, J. M. *J. Chem. Soc., Dalton Trans.* **1974**, 800−802.
(128) Bryan, R. F.; Greene, P. T. *J. Chem. Soc.* **1970**, 3064−&.
(129) Oftedal, I. *Z. Phys. Chem.* **1928**, *138*, 291−299.
(130) Leipoldt, J. G.; Coppens, P. *Inorg. Chem.* **1973**, *12*, 2269−2274.
(131) Kuchar, J.; Cernak, J.; Massa, W. *Acta Crystallogr., C* **2004**, *60*, M418−M420.
(132) Boeyens, J. C. A.; Forbes, A. G. S.; Hancock, R. D.; Wieghardt, K. *Inorg. Chem.* **1985**, *24*, 2926−2931.
(133) Beattie, J. K.; Moore, C. J. *Inorg. Chem.* **1982**, *21*, 1292−1295.